Response to Reviewers

We would like to thank all three referees for reading the manuscript so carefully and for their very helpful comments. In the following we answer all questions and reply to all comments. We have changed the paper accordingly as indicated.

The comments of the reviewers are all printed in black below while our replies are shown in blue. The page and line numbers in the reply direct to the positions in the comparison manuscript between the original and the revised version.

Referee #1:

This paper reports the results of the temperature and water vapor mixing ratio measurements with the rotational Raman lidar of the University of Hohenheim. It also describes the lidar system and the numerical simulation of the temperature measurement. The results presented in the paper are original to my knowledge and interesting. Thus, I believe that the paper can be published in ACP after minor revisions. The suggestions of the corrections are given below.

1) P28974, L12 and P28983, L9: Does the switching for the passband (changing inclination angle of the filter) of the second rotational Raman channel automatically or manually? Please explain.

Presently, the inclination angle is changed manually. Both angles are fixed with a pivot tooth. This information was added on page 11, L5.

2) P28977, L4: Please note the location (i.e. latitude, longitude, and elevation).

The location is now given in the manuscript on page 5, L1. It was 50°53'50.55'' N, 6°27'50.27''E and 110 asl.

3) P28979, Eq. (4): I think that a factor of 2 should be multiplied to P_B1 and P_B2. Also P_BWV and P_BRR in Eq. (9).

The statistical uncertainty of the background signal ΔP_B can be treated as 0, because it is determined from a very large number of measurement points in the far distance (about 2000). So the equation is correct. Please see also Behrendt et al., 2002 for more information. This reference was already given but we added a brief further explanation on page 8, L1.

4) P28980, L1: Please add the reference paper that describes how Eq. (5) is derived from Eq. (1).

Sorry, there was an error in the equation number. It should read equation 4. The Poisson error is proportional to the inverse square root of the signal intensity and therefore to those parameters which determine it. The number was corrected.

5) P28983, L15: How did you obtain the beam divergence in the polychromator? Is it based on the measurement or theoretical computation? Please explain it.

It is based on a combination of both. Experimentally, we found that the measurement of the divergence leads to results < 1° but with too high uncertainty. Thus, we made theoretical estimations and compared the results with different calculations of the calibration curve. These gave a best estimate of 0.45° for the divergence in the polychromator. This value results in good agreement when comparing the simulated and experimental curves of T(Q). We added a brief explanation to the text (page 11, L9).

6) P28983, L28: I can't find the number 37.5 m in table 2.

We record the signal with this resolution, but do not use the data for the retrieval of temperature and water vapor mixing ratio. We added this now in table 2.

7) P28984, L7: Please provide the values of dead-time of the photomultiplier tubes. It would be helpful for the users using the same type of PMT.

The dead time of the system of photomultiplier and data acquisition was determined to be 4.8 ns for both rotational Raman channels by fitting the analog and photon-counting signals. Nine years ago, a slightly larger value of 5.55 ns was used [Radlach 2009]. It was discussed with the manufacturer of the transient recorder, Licel GmbH. They confirmed this procedure. Please note that the dead-time can be influenced by both the individual data acquisition system and the individual PMT including the high-voltage supply. An explaining text was added to page 12, L4.

8) P28986, L23: Please tell me how the beam divergence affects the result of simulation. How the shape and size of the circles of temperature uncertainty in Figs. 5 and 6 change?

The changes of the calibration curves T(Q) and of the statistical uncertainties DT are larger than of the relative uncertainties DT/DTmin. We found that for beam divergences between 0.1° and 1° and our filters, the size and shape of the uncertainty plots does not change significantly: The optimum wavelengths shift by less than 0.01 nm, while the iso-lines shown in Fig 6 shift by 0.02 nm. For smaller beam divergences the curves are less circular. We added this information to the text on page 15, L2.

9) P28989, L3: Was it possible to assume that S was zero over the altitude for the low background condition?

As the background at this night-time measurement was not 0 (what would be the ideal case), S is indeed not zero. It is furthermore noteworthy that this parameter is not the same for both filters due to their shape and bandwidth. In this special case S was less than 0.1 up to 4.1 km for RR1 and 1 at 8.3 km. For the L setting of RR2 S was less than 0.1 up to 2.1 km and 1 at 4.3 km. For the H setting S was less than 0.1 up to 3.2 km and 1 at 6.6 km.
The text was rewritten to clarify this point (page 17, L19).

10) P28990, L2: Please provide the elevation angle of the lidar (i.e. vertical or slant pointing).

It was vertical (90° above horizon). This information was added to page 18, L28.

11) P28990, L8-9: Please provide the values of altitude ranges of the nocturnal boundary layer.

We cannot derive the nocturnal boundary layer height with vertical measurements of our lidar because of non-total overlap below 500 m. We therefore analyzed the radiosonde data (giving a height of 300 m at 23 UTC). The only technique to extend the measurement range to very low altitudes above ground is to use a very low elevation angle as demonstrated in Fig 16.

12) P28990, L10: Please provide the values of altitude range of the boundary layer.

The altitude of the boundary layer changes as expected through the daily circle. The methods to identify the top of the boundary layer vary (e.g. temperature gradient, gradient of aerosol content) and it is important to distinguish between convective layers and residual layers.
The top of the convective boundary layer on the 18th of May is around 1.6 km at 17 UTC. It decreases afterwards in the transition to a nocturnal boundary layer and a residual layer up to 1 km stays more or less stationary. In the morning the layer splits in several sublayers which go up to 1.3 km, whereas the boundary layer will be beneath 0.5 km as we first see it rising again at 10 UTC from underneath the measurement range. This convective layer rises up to 1.5 km at around 14 UTC.
We added this information to the text (page 19, L5 following).

13) P28991, L6: How did you obtain atmospheric pressure that is necessary to compute the potential temperature? Please explain.

Potential temperature was calculated using pressure data from the collocated radio sounding. (This information was already given a few lines below, now page 20, L16)

14) P28993, L13: Please provide the value of the relative error (in percentage) of MR.

As the relative error changes with altitude and total amount of water vapor, a graph with the relative and absolute error was added to figure 15.

15) P29000, Table 3: Is CWL2 of 352.95 (L) correct? Or is it 353.05?

Thanks for finding this error. 353.05 nm is correct. This was corrected in table 3.

16) P29001, caption of Fig.1: Please add the reference papers that report that fluorescence can affect the Stokes line based on the measurement.

We added Immler et al., 2005 as reference in the caption to figure 1. It reports fluorescence in a wider wavelength range, but also small shifts cannot be excluded.

17) P29010, Fig. 6: Please explain the possible reasons of the large difference (+/- 0.3) in Q_norm between the radiosonde and the simulation for the high background setting below 265 K.

Please find a detailed explanation in the response to referee #2. It can be found on page 9 in this document.

18) P29014, Fig. 13: Please point the time when you changed the setting of IF3 between the high and low background mode.

The setting was changed at 20 UTC on May 18th and 5 UTC on May 19th. This was added to the text on page 19, L1.

19) P29014, Fig. 13: The temperature gradient below 1 km for 14-16 UTC on 19 May and 16-17 UTC were super adiabatic (-2.0 K/100 m). Do you think they were real or in measurement error? Please comment on it.

Another check of the data showed small remaining overlap effects which resulted in these super-adiabatic values. Therefore the analysis was revised and after correction the values found in the specified altitude ranges are around -1 K/100 m which is more realistic as it is close to the adiabatic lapse rate. The figure was exchanged.

20) P29015, Fig.14: We can see that there were many spots of high +/- 3 K/100 m) temperature gradients for a few minutes were present at an altitude of 1.5 km over the measurement period. Were it statistically significant (within the measurement error)?

With a range resolution of 105 m and time resolution of 50 s for each profile, the statistical error is around 4 K/100m at 1.5 km. Therefore, corresponding fluctuations are expected. Nevertheless, these high-resolution data show that the highest gradients were present at the top of the convective boundary and that the RRL is capable of detecting them. The caption of the figure and the text were slightly extended to give this information. Additionally we added the statistical error and a plot with a lower time resolution of 5 minutes reducing the statistical error to 1.1 K/100 m at 1.5 km.

Referee #2:

This paper describes the design and construction of a new lidar system used to profile the boundary layer during night-time and daytime, and presents some preliminary results and comparison with radiosondes. It is a carefully-written paper which with minor revision should be suitable for publication in ACP.

My most serious comment concerns the design of the tilted filter which allows the two different wavelength bands to be used for the second rotational Raman filter, depending on the background noise. This is the main result of the paper, but it is simply presented as a fact and not discussed. The calculations and results pertain to the particular lidar used in this study and it is not clear how they transfer to other lidars, and thus be of general use to the community. Basically, the question is whether this degree of complexity in lidar design is worth it, given the result in fig 12 that under conditions of (very) high background noise the high-background system only provides a really significant improvement in temperature error above about 4 km – below that the improvement is either <10 % or not an improvement at all (below 1 km). For a system designed for boundary layer measurements this does not appear to me to be worth it. A section in the concluding section discussing the significance of the results is required.

A section was added to explain the significance of the results and how they can be applied to other systems (page 22). As our main research topic is turbulence in the boundary layer, we believe that this technically quite simple and cheap concept is worth the effort. A reduction of the statistical error by 10% at daytime may not seem large, but corresponds for example to an increase in laser power of 30%. Alternatively, it means that the averaging time can be 30% shorter for the same error. Originally our goal was to improve the low background measurement capability as the lidar was designed for daytime measurements already. As described in the paper, this was achieved with around 70% less uncertainty in low altitudes. The improvement of daytime measurements with the low background setting in low altitudes was not expected, but noted.

Concerning the application to other systems: It is true that strictly speaking, the results are valid for a specific laser wavelength and specific filter widths. But the same concept can be adapted to any system. And as the results do not change dramatically for slightly different parameters (see also comment above to reviewer 1), one can easily use our results for orientation. Especially figure 6 can be helpful as there is all information collected. To determine the exact wavelength pairs, the simulation has to be repeated for other system parameters but this is straightforward. We added a corresponding comment to the text on page 22.

Minor points (mainly language corrections):

l.40 ‘superior’ rather than ‘advantageous’

Corrected (page 3, L10)

l.65 ‘DIAL, whose self-calibrating property leads to’

Corrected (page 4, L10)

l.68 ‘system already contains’

Corrected (page 4, L13)

l.73 ‘DIAL, from which are presented in Muppa et al. (2014) and Spaeth et al. (2014).’

Corrected (page 4, L20)

l.75 ‘forecasts’

Corrected (page 4, L21)

l.79 ‘The area already had’

Corrected (page 4, L26)

l.81 ‘and thus provided data set of thermodynamic properties for the atmosphere.’

Corrected (page 4, L29)

l.84 Say by how much the site was elevated from its surroundings

It was added to page 5, L4, that the site was 10 to 15 m above the surroundings in main measurement direction.

l.89 At this point you have not introduced the ‘novel switch’ so this sentence makes no sense to the reader. Better to just say ‘It is the goal of this paper’

The sentence was rearranged (page 5, L9).

l.92 I’m not sure what you’re trying to say. Is it ‘Except for two night-long measurements, the lidar was only operated during daylight hours when there was no rain or continuous dense cloud cover’?

Our main measurement goal was the convective boundary layer so we measured mostly during daytime. The given sentence should give the reader that information and additionally what the exceptions were. We interrupted measurements due to rain or if the clouds were dense and low. Additional to the daytime measurements we performed measurements during two nights between consecutive IOP days. The text was changed accordingly on page 5, L14.

l.94 During one day and one night, the lidar was pointing at a low elevation above the ground’

Corrected (page 5, L17)

l.95 '..started at the beginning..'

Corrected (page 5, L18)

l.96 ' – and also'

Corrected (page 5, L20)

l.102 delete 'also'

Corrected (page 5, L26)

l.107 delete 'short time of'. This sentence contradicts line 333 where you say it takes 5 minutes to change the filter position.

Thanks, it takes about 5 minutes to change the configuration. This was corrected in the text (page 6, L4).

l.121 ' assumptions about'

Corrected (page 6, L17)

l.122 'Figure 2 shows how the depend on the temperature'

Corrected (page 6, L17)

l.124 'CWL2: one for (L) and one for.'

Corrected (page 6, L20)

l.126 'has a different slope.. formulae'

The Oxford dictionary says that 'formulas' as well as 'formulae' are the plural of 'formula'.

l.128 'we use mostly'

Corrected (page 6, L24)

l.129 RR!, and a and b'

Corrected (page 7, L4)

l.132 'measurements are made over a'

Corrected (page 7, L7)

l.133 delete But

Corrected (page 7, L8)

l.138 'photon-counting'

Corrected (page 7, L13)

l.143 Seems to have been left over from a previous draft. Equation 1 has nothing to do with the symbols in equation 5. A proper explanation is required.

Thanks, it is right that the link is to the wrong equation. The correct equation is formula 4. It was changed in the manuscript. Please see also response referee #1.

l.147, equation 6. I don't see where the factor of 2 comes from. A gradient is calculated from (T1-T2)/(r1-r2). In this case T1 and T2 are independent measurements so the error in (T1-T2) is SQRT(deltaT1^2 + deltaT2^2), i.e. the errors are added in quadrature. If the gradient is evaluated over a small enough height range the two deltaTs will be the same – and equation 2 should have SQRT(2) not 2. If you have a different error calculation this should be fully described.

Thanks! The square root was indeed missing. Equation 6 was corrected.

l.165 Poisson

Corrected (page 9, L6)

l.169 citations are wrong here – these are in-line citations and should not be parenthesised.

Corrected (page 9, L10)

l.182 and 186 Nd-YAG laser

As 'Nd:YAG' is the more common spelling, we did not change it to Nd-YAG.

l.237 photon-counting

Corrected (page 12, L3 and elsewhere)

l.246 'To determine'

Corrected (page 12, L18)

l.248 'this scaling'

Corrected (page 12, L21)

l.250 'signals, a temperature-independent molecular'

Corrected (page 12, L26)

l.252 'as a reference'

Corrected (page 12, L28)

l.294 'During daytime, S for a well-designed'

Corrected (page 14, L17)

p.307 ‘limited to 354.2 nm and smaller to ensure that the elastic signal is blocked for this channel’

Corrected (page 15, L8)

l.311 ‘optimum, and therefore.’

Corrected (page 15, L13)

l.342 ‘radiosonde at the same height’

Corrected (page 16, L23)

l.346 ‘present at higher altitudes’

This sentence is no longer in the manuscript due to the changes suggested in the following comment.

l.346. This throwaway explanation of the discrepancy in fig.9 is not acceptable. The fact that the performance of the setting is not optimised does not explain why the theoretical curve departs from the measurements, and 3% is a big discrepancy (it corresponds to several K). Perhaps the drift of the radiosonde away from the lidar is a contributor – but in that case why is the agreement so good for the low-noise case? Temperature in the free troposphere doesn’t usually vary rapidly with horizontal distance (or radiosondes wouldn’t be much use for weather forecasting).

There is a small uncertainty in the angle of incidence in which the interference filters are aligned. The simulation of Q values was based on the values we wanted to align to. Now, the comparison of the experimental calibration with the theoretically expected one indeed gives some indication that the angles of incidence where in fact slightly different. Motivated by the reviewers’ comments, we iterated the simulations of the calibration curve and found that angle of incidence of 4.8° (instead of 4.5°) for the high-background setting of RR2 filter (IF 3) shows very close agreement: All points are within the 1-sigma uncertainties except those at the top of the ABL where the atmospheric temperature variations are largest. We thus conclude that this revised angle is correct and have consequently revised all related descriptions in the new version: The figures 1, 5, 6 and 9 were exchanged to take account of the new simulation values, Table 1 and 3 were corrected, and the text describing figure 9 (page 16, L21ff) was changed accordingly.

l.350 ‘with the two settings’

Corrected (page 17, L10)

l.357 ‘As expected’

Corrected (page 17, L23)

l.364 night-time

Corrected (page 18, L4)

l.366 you are arguing here that the H setting shows less uncertainty at low temperatures than the L setting. I think I understand but you need to explain this better, perhaps with reference to fig. 6.

The explanation on page 18, L6 was extended and a reference to figure 6 is given.

l.366 ‘At low altitudes’

Corrected (page 18, L6)

l.369 ‘an advantage’ or ‘advantageous’

Corrected (page 18, L14)

l.372 ‘shows an advantage lies above 1 km unless.’

Corrected (page 18, L18)

l.387 ‘UTC, which can be seen’

Corrected (page 19, L9)

l.393 ‘A high positive gradient indicates a temperature inversion.’

Corrected (page 19, L18)

l.395 why is it surprising?

‘Surprising’ was exchanged to ’remarkable’(page 19, L19). We expected to find the highest temperature gradient values at the top of the convective boundary layer or at this time of the day closer to the ground.

l.430 ‘elevated above its surroundings by’

Corrected (page 21, L15)

l.431 ‘ range to height’

Corrected (page 21, L16)

l.434 ‘..to the vertical’

Corrected (page 21, L20)

l.455 ‘commonly used’

Corrected (page 23, L3)

l.654 prism

Corrected (page 33, caption figure 3)

l.664 temperature-independent

Corrected (page 34, caption figure 4)

l.770 ‘..better performance for the’

Corrected (page 44, caption figure 12)

l.772 ‘..significant at lower’

Corrected (page 44, caption figure 12)

Referee #3

The paper presents measurements of temperature and humidity taken during the HOPE campaign with a Raman lidar using the rotational Raman technique. A novel feature of the system is that it can measure in two configurations, optimized for high and low background conditions, respectively. The performance of the two configurations and the capability to measure water vapor and temperature gradients simultaneously are demonstrated.

The paper is well written and the content is innovative and scientifically relevant and well presented. I recommend the paper for publication after minor revisions as specified below.

General comments

The text of the paper, in particular abstract and summary&outlook, should be more quantitative when explaining the benefit of the two background configurations. For example formulations like "significant advance", "advantages of new background configuration" and "the high background setting shows low statistical error" should be quantified.

As suggested by the reviewer, we rewrote the mentioned passages and give now more quantitative statements.

Generally, the first person plural is not good scientific language and should be avoided.

We found controversial opinions if the first person plural can be used in scientific English (e.g., the Science magazine states that passive sentences should be avoided and active “we”-sentences should be used, www.sciencemag.org/about/authors/prep/res/style.dtl). Nonetheless the use of ‘we’ was omitted in the revised version if possible.

Specific comments

p28976, l7: this is a very incomplete list of references. Either put "e.g." at the beginning or add the missing references.

The list should give only a rough idea about the work in this field as this is not one of the main topics. Therefore “e.g.” was added as suggested (page 4, L6).

p28979, l3: specify that it is referred to corrected (background, saturation,..) signals.

Done on page 7, L3.

p28980, l14: please specify how saturation effects are accounted for.

We guess the referee relates to saturation effects in the photomultipliers. As we use for the data analysis only the analog signal (compare page 11, L23), the photon-

counting dead time correction applies only for data used to estimate the statistical error.

p28984, l8: explain how the averaging affects the statistical errors according to equation 4,5 and 9.

According to equation 4 an average factor of 2 in time and range results in a decrease of the statistical error of a factor sqrt(2). This applies both to temperature and water vapor mixing ratio. The link to equation 5 was added to the manuscript (page 12, L11).

P28984, l17: This approach needs to be justified and validated. Behrendt et al. 2014 does not give any justification or validation and cannot be referred to, here.

We added as reference 'Whiteman et al., 2006'(page 12, L20) in which the use of analog data as virtual photons is described. They did also an error analysis and a validation of the method. It was also added that this approach only includes the signal noise error and not the total statistical error (page 12, L22).

P28985, l20: "This first..." it is not quite clear what the authors want to say here.

Corrected to "RR1 channel" on page 13, L23.

P28986, l8: remove the unit from the equation.

As the equation expects as input parameter the bandwidth of the filter in units of m, the unit is necessary.

P28989, l6: "Absolute values..." this phrase is not clear.

It was meant that in general the absolute error values with high background are higher compared to the absolute error values with low background conditions. This was clarified in the text (page 17, L25).

P28991, l21: The layer at 2 km seems to contain no humidity at all. Not even the error bars reach positive values. Could the authors comment on that?

Figure 15 was changed so that all measurement values with their 1-sigma statistical error bars are now visible.

Of course, negative values of the water vapor mixing ratio are physically not possible. But in this case, they appear as measured values as a consequence of the small signal to noise ratio due to the small amount of water vapor at this height resulting in a signal which was not statistically distinguishable from the daylight background. Note that the 1-sigma statistical range indicates a probability of 68 % that the real value in found within. We do not want to shift these values to 0 because if doing so, the mean of the data is biased. This is now also explained briefly in the text (page 20, L26).

p28991, l24: For a non lidar person this phrase is close to incomprehensible. "Poisson statistics" is not, and should not become, a generally accepted term for "signal noise". In particular not when analog signals are considered (see comment above).

It was clarified that it is in fact the noise error. A link to equation 4 is given now page 21, L5.

P28992, l15: As a suggestion, this could be validated with a microwave radiometer, if available on site. In the first few hundreds of meters the vertical resolution is good enough to measure such gradients.

The microwave radiometer which was available on site was a system of HATPRO with vertical data steps of 50 m. This step width together with the large weighting function and large field-of-view of the radiometer makes it impossible to resolve the gradients present in this case. Therefore we decided not to include the radiometer profile here.

P28993, l3: Do the authors mean "lower"? Give a number how low "low" (or lower) is.

It was meant low/small in comparison with the absolute values of the measured variable. For example 0.3 K in a twenty minute average temperature like shown in figure 11.

As the whole section was rewritten this sentence does not longer exist. We hope that the referee agrees to the new text.

p28993, l11: "convenient" for what? Later in this phrase, be clear that it is referred to the statistical error only.

Convenient was replaced with an explanation. It was clarified that the statistical error is meant (page 23, L6).

‘Convenient’ under the aspect that it is possible to observe processes in a temporal resolution which is needed e.g. turbulent eddies (10 s profiles) or the evolution of a convective boundary layer. If we want to ensure that the statistical error is less than 0.1 K for example, we can decrease either the spatial or temporal resolution.

Manuscript prepared for Atmos. Chem. Phys. Discuss.
with version 2014/09/16 7.15 Copernicus papers of the LaTeX class copernicus.cls.
Date: 6 February 2015

Temperature profiling of the atmospheric boundary layer with rotational Raman lidar during the HD(CP)^2 observational prototype experiment

E. Hammann[1], A. Behrendt[1], F. Le Mounier[2], and V. Wulfmeyer[1]

[1]University of Hohenheim, Institute of Physics and Meteorology, Garbenstrasse 30, 70599 Stuttgart, Germany
[2]Laboratoire de Météorologie Dynamique, C.N.R.S, Paris, France

Correspondence to: E. Hammann (eva.hammann@uni-hohenheim.de)

Abstract

The temperature measurements of the Rotational Raman Lidar of the University of Hohenheim (UHOH RRL) during the High Definition of Clouds and Precipitation for advancing Climate Prediction (HD(CP)^2) Prototype Experiment (HOPE) in April and May 2013 are discussed. The lidar consists of a frequency-tripled Nd:YAG laser at 355 nm with 10 W average power at 50 Hz, a two-mirror scanner, a 40 cm receiving telescope and a highly efficient polychromator with cascading interference filters for separating four signals: the elastic backscatter signal, two rotational Raman signals with different temperature dependence, and the vibrational Raman signal of water vapor. The main measurement variable of the UHOH RRL is temperature. For the HOPE campaign, the lidar receiver was optimized for high and low background levels, respectively, with a novel switch for the passband of the second rotational Raman channel. The instrument delivers atmospheric profiles of water vapor mixing ratio as well as particle backscatter coefficient and particle extinction coefficient as further products. As examples for the measurement performance, measurements of the temperature gradient and water vapor mixing ratio revealing the development of the atmospheric boundary layer within 25 h are presented. As expected from simulations, a ~~significant advance~~ reduction of the measurement uncertainty of 70 percent during nighttime was achieved with the new low-background setting. A two-mirror scanner allows for measurements in different directions. When pointing the scanner to low elevation, measurements close to the ground become possible which are otherwise impossible due to the non-total overlap of laser beam and receiving telescope field-of-view in the near range. ~~We present an~~ An example of a low-level temperature measurement is presented which resolves the temperature gradient at the top of the stable nighttime boundary layer a hundred meters above the ground.

1 Introduction

In recent years, different techniques for measuring the atmospheric temperature profile with lidar have been developed, namely the rotational Raman technique, the integration technique (using elastic and Raman signals, respectively), the resonance fluorescence technique as well as the high-spectral resolution lidar (HSRL) technique and differential absorption lidar (DIAL) (see Behrendt, 2005 for an overview). For daytime measurements in the troposphere, rotational Raman lidar (RRL) is presently the most reliable technique. Its capabilities in providing temperature profiles with high temporal and spatial resolution and low systematic and noise errors at night- and daytime even within aerosol layers and thin clouds are ~~advantageous~~ superior so far to all other techniques particularly if measurements from the surface to the lower troposphere are concerned (Behrendt and Reichardt, 2000; Behrendt et al., 2002, 2004; Di Girolamo et al., 2004; Arshinov et al., 2005; Radlach et al., 2008).

Most rotational Raman systems operate at wavelengths of 532 or 355 nm, the second and third harmonic wavelengths of Nd:YAG lasers. UV systems are able to perform daytime measurements with lower uncertainties due to the higher backscatter cross section and less solar background (Zeyn et al., 1996; Behrendt et al., 2005). The rotational Raman lidars of NASA Goddard Space Flight Center (Di Girolamo et al., 2004), of University of Hohenheim (Radlach et al., 2008), of University of Basilicata (Di Girolamo et al., 2009), of Xi'an University (Mao et al., 2009) and of Hampton University (Su et al., 2013) all operate in the UV with interference-filter polychromators. Rotational Raman lidar at 532 nm show lower performance at daytime but reach larger range at night than an UV system due to the higher laser power available at 532 nm compared to 355 nm, higher efficiency in signal separation, and lower atmospheric extinction. Some of the systems at 532 nm are also based on interference filters (Behrendt and Reichardt, 2000; Behrendt et al., 2002, 2004; Achtert et al., 2013) and some employ double-grating polychromators (Balin et al., 2004; Arshinov et al., 2005).

Daytime temperature measurements are the main focus of the RRL of UHOH. But besides temperature also the particle backscatter coefficient and the particle extinction coefficient can be measured independently. Furthermore, the system was extended recently with a water vapor Raman channel. For water vapor measurements, two different lidar techniques are available: the DIAL technique and the Raman lidar technique. While water vapor Raman lidar uses the vibrational Raman backscatter signals of water vapor (e.g. Melfi et al., 1969; Whiteman et al., 1992; Turner et al., 1999; Leblanc and McDermid, 2008), the DIAL technique (Schotland, 1974; Wulfmeyer and Bösenberg, 1998; Behrendt et al., 2009; Wagner et al., 2013) relies on the different absorption of water vapor at two near-by wavelengths. In contrast to water vapor DIAL~~with its~~ , whose self-calibrating property ~~, which~~ leads to a high accuracy of the measurements (Bhawar et al., 2011), a water vapor Raman lidar has to be calibrated and shows also lower performance at daytime. However, the laser transmitter is less complex and if a certain lidar system ~~contains already~~ already contains rotational Raman channels, only one more detection channel is needed to derive in addition the water vapor mixing ratio (Behrendt et al., 2002). Thus ~~we have~~ it was decided to extend the UHOH RRL with a water vapor channel. Furthermore, this capability permits relative humidity measurements, which are, e.g., useful for aerosol (Wulfmeyer and Feingold, 2000) and convection initiation studies (Behrendt et al., 2011; Corsmeier et al., 2011). In parallel to the RRL, the UHOH has developed also a water vapor DIAL, from which recent measurements are presented in ~~(~~Muppa et al. ~~,~~ (2014~~;~~) and Späth et al. ~~,~~ (2014).

Within the HD(CP)^2 project, a new model for high-resolution weather ~~forecast~~ forecasts will be developed (Stevens and Bony, 2013) and other model systems will be tested (Schwitalla and Wulfmeyer, 2014). To verify the model, high resolution data sets are required. The HD(CP)^2 observation prototype experiment (HOPE) providing such a data set took place during April and May 2013 in the area around the Research Center Jülich in Northwest Germany. The area ~~had already~~ already had an existing infrastructure of dense standard meteorological instrumentation.

Both system of UHOH have been operated together in the HOPE field campaign and ~~provided thus~~ thus provided a synergetic data set of ~~the~~ thermodynamic properties of the

atmosphere. The lidars were located at one supersite (50°53'50.55"N, 6°27'50.27"E, 110 m above sea level) close to the village of Hambach together with the KITcube, an instrument suite of the Karlsruhe Institute of Technology (KIT) (Kalthoff et al., 2013). The site was ~~slightly~~ on a hillside and elevated to the surrounding by 10 to 15 m. The RRL and the Water Vapor DIAL of UHOH were collocated with a Doppler lidar from KIT to acquire a complete data set of temperature, water vapor content and vertical wind for the determination of fluxes of sensible and latent heat (e.g., Behrendt et al., 2011). It was also the launch site for ~~radiosoundings~~radio soundings.

~~Besides presenting the novel switch for low- and high-background RRL, it~~ It is the goal of this paper to introduce the measurement performance of the UHOH RRL during HOPE and present highlights of the measurements. One highlight was the application of a novel switch for low- and high-background RRL. During the 18 intensive observation periods more than 200 h of measurements were collected. ~~Except of two night-long measurements, only~~ Measurements took place in the time between sunrise and sunset ~~was covered in absence~~ and were stopped in case of rain or continuing dense cloud cover. In addition there were two night-long measurements. On one day, RHI (Range-Height-Indicator) scans were performed. ~~One~~ During one day and one night, the lidar was pointing ~~in~~ at a low elevation above the ground. Water vapor measurement started ~~in~~ at the beginning of May, therefore only 100 h of water vapor data are available. Case studies using the combination of data from the instrument set – and also from the other two supersites – are in preparation and will be presented later based on the results shown here.

~~Our~~ The main research interest of our institute is land–surface–atmosphere feedback, which requires measurements of land–surface exchange, the surface layer, the atmospheric boundary layer, and the lower free troposphere. For investigating not only mean profiles or mean 3-dimensional fields but also the turbulent features of the convective boundary layer, instruments providing data with high temporal and spatial resolution ~~also~~ in conditions of high-background light are needed. The rotational Raman lidar of UHOH was optimized for such conditions. A new technical feature~~we~~, which was implemented during the HOPE campaign, was a switch to optimize the performance of the temperature measurements for

low and high background conditions, respectively. ~~We made detailed simulations~~ Detailed simulations were performed which showed that it is favorable to use another pair of filter center wavelengths in low background conditions than in cases with high solar background. The change between the settings can be made in ~~short time of~~ a few ~~seconds~~minutes. Thus, it was possible to switch easily between the settings and acquire continuous time periods of data which included such changes.

This paper is structured as follows: In Sect. 2 the new setup of the UHOH RRL is explained. Also the simulations for two settings for the second rotational Raman channel are presented. Section 3 discusses the experimental results of the new system. Section 4 gives a short summary.

2 Methods and performance simulations

2.1 Methods

The rotational Raman lidar of UHOH makes use of the rotational Raman technique for deriving atmospheric temperature profiles (Cooney, 1972). Two parts of the rotational Raman spectrum of air with different temperature dependency are acquired (see Fig. 1). By taking the ratio of the two signals (Fig. 2) and calibrating it, the temperature is obtained without further assumptions ~~on~~ about the state of the atmosphere. Figure 2 shows how the rotational Raman signals P_{RR1} and P_{RR2} ~~in dependency of~~ depend on the temperature. For P_{RR2} there are the two settings shown in Fig. 1 with different central wavelengths CWL2: ~~One~~ one for low background (L) ~~,~~ and one for high background (H) conditions. The setting L results in a lower signal intensity in the second Raman channel. Also the ratio Q between P_{RR2} and P_{RR1} is lower and has a different slope than the one for the H setting. There are several formulas in use for the calibration (Behrendt and Reichardt, 2000; Behrendt, 2005). For temperatures measurements up to a few km altitude, ~~we are using mostly~~ the following

equation can be used

$$Q(T) = \exp\left(a - \frac{b}{T}\right) \tag{1}$$

where Q is the ratio between the background corrected signals in the Raman channels RR2 and RR1, and a and b are calibration constants. This equation is exact for the ratio of two single rotational Raman lines. If several rotational Raman lines are extracted by the two channels, more complicated equations with more constants are needed when temperature measurements are made over a larger range of temperatures ~~are made~~ (Behrendt and Reichardt, 2000; Behrendt, 2005). ~~But this is not our~~ This is not the purpose here so that this equation can still be used resulting in a high accuracy of the inversion. Therefore ~~we can get~~ the atmospheric temperature can be derived from Q by rearranging Eq. (1) to

$$T = \frac{b}{a - \ln(Q)}. \tag{2}$$

The statistical error of the temperature measurements can be determined from the signal intensities of the ~~photo counting~~ photon-counting data and applying Poisson statistics. For a signal with count number *s,* the 1-σ statistical error is

$$\Delta s = \sqrt{s}. \tag{3}$$

This results in a noise error for the temperature ΔT (Behrendt et al., 2002) of

$$\Delta T = \frac{\partial T}{\partial Q} Q \sqrt{\frac{P_{\mathrm{RR1}} + P_{\mathrm{B1}}}{P_{\mathrm{RR1}}^2} + \frac{P_{\mathrm{RR2}} + P_{\mathrm{B2}}}{P_{\mathrm{RR2}}^2}}. \tag{4}$$

P_{RR1} is the background-corrected signal in the first Raman channel, P_{B1} the background in this channel, P_{RR2} and P_{B2} are the same for the second Raman channel. This equation is

valid if ΔP_B is zero, which is a valid approximation if the background is calculated from a high number of bins. One can see from Eq. (~~1~~4) that the error ΔT scales with

$$\Delta T \sim \frac{1}{\sqrt{PtA\eta}} \tag{5}$$

where P is the laser power, t the integration time, A the telescope area and η the overall detection efficiency.

The statistical error ΔT_{Grad} of a temperature gradient measurements is then

$$\Delta T_{\text{Grad}} = \frac{2\Delta T}{\Delta r} \frac{\sqrt{2}\Delta T}{\Delta r} \tag{6}$$

with Δr the range interval over which the gradient was calculated.

The two rotational Raman signals can also be used to form a temperature-independent reference signal P_{RR} for the determination of the particle backscatter coefficient, the particle extinction coefficient or the water vapor mixing ratio (Behrendt et al., 2002, 2004).

The water vapor mixing ratio MR at a distance r is calculated with

$$\text{MR}(r) = C \cdot \frac{P_{\text{WV}}(r)}{P_{\text{RR}}(r)} \Gamma(r) \tag{7}$$

where C is a calibration constant, P_{WV} and P_{RR} are the background-corrected signals of the vibrational Raman line of water vapor and the rotational Raman lines of nitrogen and oxygen, respectively (Whiteman et al., 1992; Sherlock et al., 1999). $\Gamma(r)$ is a correction for the different atmospheric extinction Γ at the two wavelengths λ_{N_2} and $\lambda_{\text{H}_2\text{O}}$

$$\Gamma(r) = \frac{\exp\left[-\int_{r_0}^{r} \alpha\left(\lambda_{\text{N}_2}, r'\right) \mathrm{d}r'\right]}{\exp\left[-\int_{r_0}^{r} \alpha\left(\lambda_{\text{H}_2\text{O}}, r'\right) \mathrm{d}r'\right]}. \tag{8}$$

To determine the calibration constant C, ~~we use~~ a collocated radio sounding can be used. It was found that a correction for the different extinction coefficient of the two wavelengths

is negligible for ranges of up to a few kilometers because the difference is less than 0.1 % up to 3 km.

The statistical error of the water vapor measurements can be calculated with Poisson statistics and one gets

$$\Delta \mathrm{MR} = C \frac{P_{\mathrm{WV}}}{P_{\mathrm{RR}}} \sqrt{\frac{P_{\mathrm{WV}} + P_{\mathrm{BWV}}}{P_{\mathrm{WV}}^2} + \frac{P_{\mathrm{RR}} + P_{\mathrm{BRR}}}{P_{\mathrm{RR}}^2}}. \quad (9)$$

While the error analysis based on Poisson statistics determines the so-called shot noise errors, the total statistical error can be estimated with an analysis of the turbulent fluctuations in the atmosphere (Lenschow et al., 2000). For this, data with high temporal resolution is needed in order to resolve the time scale of these fluctuations. The method based on the analysis of the autocovariance function was developed in (Senff et al., (1994;) and Wulfmeyer et al., (1999a, b), and summarized in (Lenschow et al., (2000). Recently, this technique was applied to WV DIAL (e.g., Muppa et al., 2014) and Doppler lidar data (Lenschow et al., 2012), elastic backscatter lidar data (Pal et al., 2010), and water vapor Raman lidar data (Wulfmeyer et al., 2010; Turner et al., 2014a, b). Recently it was applied for the first time to temperature lidar data by using measurements of the UHOH RRL during HOPE (Behrendt et al., 2014). The comparison between the errors derived with Poisson statistics and turbulence analysis confirms that the total statistical error is mainly due to photon shot noise.

2.2 Current setup

The rotational Raman lidar of UHOH aims at measurements in the atmospheric boundary layer and lower free troposphere during daytime. A scheme of the setup is shown in Fig. 3. As laser source an injection-seeded frequency-tripled Nd:YAG-laser(Spectra Physics GCR290-50) is used. Only the third harmonic radiation at 354.83 nm is transmitted into the atmosphere. The human eye is less sensitive to UV wavelengths than to wavelengths in the visible spectrum and therefore eye safety is fulfilled already at a smaller distances for

UV lidars than for lidars using e.g., the second harmonic radiation of a Nd:YAG laser. In consequence, the first and second harmonic are separated in ~~our~~ the transmitter from the third using a Pellin-Broca prism and directed into beam dumps. The separation by a prism is preferable to a beam splitter due to the fact that the wavelengths are separated spatially and definitely no radiation at the other wavelengths is remaining in the outgoing light. The transmitted power in the UV is around 10 W at a repetition rate of 50 Hz. The beam is expanded by a factor of 6.5 to prevent damage on the transmitting optics and to achieve eye safety in less than 400 m distance (taking also hotspots in the beam profile into account). The expanded beam is directed via three mirrors (10 cm diameter) onto the first mirror of the beam steering unit. Together with a second mirror, this setup enables us to direct the beam to any azimuth and elevation angle of interest. The whole system is mounted on a mobile platform which can be moved to different measurement sites for field campaigns.

The receiving telescope is of Ritchey–Chrétien–Cassegrain type. Its primary mirror has a diameter of 40 cm. To reduce the daylight background, the focused signal passes a pinhole with selectable diameter. The diameter was set to 3 mm during the HOPE campaign which results in a full field of view of 0.75 mrad. After passing this field stop, the light is parallelized with a lens and then split by a dichroic beam splitter: while light with wavelengths shorter than 375 nm is transmitted into the main receiver unit, longer wavelengths are reflected. The vibrational-rotational Raman signal of water vapor excited by 354.83 nm is shifted by wavenumbers around 3657.05 cm^{-1} (e.g., Avila et al., 2004) from the excitation wavelength and is thus around 407.7 nm ~~in our case~~ and obtained from the light reflected by the beam splitter. The transmission efficiency of the beam splitter is 0.93 for 355 nm and 0.02 for 408 nm. Reflectivity at 408 nm is above 0.95.

The signal transmitted by the beam splitter passes a daylight reducing filter IF0 (Eureca, peak transmission of 0.56) and enters the main part of the receiver for the detection of the elastic and rotational Raman signals, which follows a cascading scheme (Behrendt and Reichardt, 2000; Behrendt et al., 2002, 2004; Radlach et al., 2008). In front of the first rotational Raman channel, two identical interference filters IF2a and IF2b are used to achieve sufficient suppression of the elastic signal. In Table 1 all filter parameters are listed. The first

filter pair has a transmission of 0.34 for 354.15 nm and 10^{-6} for 354.83 nm. The passbands have a full width at half maximum of 0.3 nm. The filter for extracting the second rotational Raman signal can be toggled between two distinct angles to optimize the performance of temperature measurements during conditions of high and low background, respectively (see below). For the time being, the change of setting has to be done manually, but the angles are fixed by a pivot tooth. It has a peak transmission of 0.52 and is 0.5 nm broad. The angles of incidence are 6° for the interference filters IF2a and b and ~~4.5~~ 4.8 and 6.2° for the second interference filter for the high- and low-background setting, respectively. The beam divergence in the polychromator is 0.45° as determined by experimentally validated ray tracing calculations. All narrowband interference filters were manufactured by Materion, Barr Precision Optics & Thin Film Coating. As photomultiplier for the rotational Raman signals a Hamamatsu R1924P is used. The elastic channel is equipped with a neutral density filter (transmission of 0.2) to prevent saturation of the photomultiplier (Hamamatsu R7400-U02) in the presence of optically thick clouds in the near-range.

In the branch of the water vapor channel, an interference filter (IF4) transmits the desired wavelength range, details see Table 1. The total suppression has an efficiency of 10^{-8} for 355 nm and 10^{-6} for other wavelengths. Signal is focused on a photomultiplier (Hamamatsu R1924P) for detection.

Presently, ~~we are using~~ two data acquisition systems are used for the four lidar signals. First, there is a transient recorder (LICEL GmbH, Berlin) with three acquisition channels. Each photomultiplier signal is recorded in analog mode with 3.75 m range resolution and in ~~photo-counting~~ photon-counting mode with range resolutions of 3.75 m and 37.5 m (see Table 2). The measurement data shown here were all derived with the analog data. In standard operation, backscatter signals of 500 shots are averaged to get a profile with 10 s integration time. At the beginning of the HOPE campaign, the elastic signal and the two Raman channels were recorded with this system. From early May on the water vapor detection channel signal was implemented and its signal was recorded with the LICEL data acquisition instead of the elastic signal. The strong elastic signal was then stored with a transient

recorder system (Compuscope 14100 card of GaGe Applied Inc.) with resolutions of 3 m and 1 s but only in analog mode.

The data analysis contains the following steps. First, the ~~photo-counting~~ photon-counting data are corrected for photomultiplier dead-time effects. A dead-time of 4.8 ns was determined by comparing analog with photon-counting signal and used for the correction. It has to be noted that the dead-time is not only influenced by the photomultiplier alone, but also depends on the data acquisition system. Then, the signals are background corrected and smoothed in range and time with gliding average lengths that depend on the noise conditions and application. E.g., for turbulence analysis (Behrendt et al., 2014) high temporal resolution of 10 s is needed while for studies of the temperature gradient a low statistical error is essential. How the statistical error is affected by the averaging can be seen in Eq. (5). Temperature and other data products are then determined with the analog and photon-counting signals separately and merged afterwards if needed. We found that the alternative approach of first merging the analog and photon-counting signals and then deriving the data products in a second step with the merged signals (Newsom et al., 2009) results in unstable temperature calibration functions because the merging procedure produces small erroneous fluctuations which influence the temperature measurements critically. ~~Only for determining~~ To determine the statistical uncertainties of the data, ~~we scale~~ the analog data ~~to the photon counting~~ are scaled to the photon-counting signals in order to attribute virtual count rates to the analog data ~~.~~(Whiteman et al., 2006). It turned out that ~~these~~ this scaling results in accurate shot noise error estimates also for the analog data~~(~~. In Behrendt et al., 2014 ~~).~~ it is shown that the total statistical error depends mainly on the noise error. It is therefore possible to obtain a good error estimation by calculating the shot noise error through Poisson statistics.

From the combination of the two temperature-dependent signals~~a temperature independent~~ , a temperature-independent molecular reference signal can also be obtained. The weighted sum of the signals with a weighting factor that depends on the system characteristics (Behrendt et al., 2002) can be used as a reference signal for the calculation of the water vapor mixing ratio MR, particle backscatter coefficient β and extinction coefficient α

(see also Fig. 4); no further vibrational nitrogen Raman signal like used in other Raman lidar systems is needed. It should also be noted that the statistical uncertainty of the rotational Raman reference signals is lower than the uncertainty of the weaker nitrogen vibrational Raman signal.

The measured temperature profiles can be used to further derive, e.g., profiles of potential temperature θ, temperature gradients, variance or other higher-order moments of turbulent temperature fluctuations. If profiles of vertical wind w are available with high temporal resolution, e.g., from a Doppler lidar the sensible heat flux can be calculated. Also other products like buoyancy (Corsmeier et al., 2011), CAPE (Convective Available Potential Energy) and CIN (Convective Inhibition) (Behrendt et al., 2011) are possible.

2.3 Determination of optimum configurations for low and high background

A switch for the central wavelength of the interference filter of the second rotational-Raman-channel was introduced during the HOPE campaign. By selecting lines for the second (high J) rotational Raman backscatter channel with larger spectral distance to the excitation wavelength one can enhance the temperature sensitivity of the system. But while these lines are more temperature sensitive, they are also weaker in intensity. Consequently, there is a tradeoff between temperature dependence and signal intensity which results in optimum settings which depend on the signal background relative to the Raman signal intensities (Radlach, 2009). In the following, ~~we present~~ refined simulation results on this problem of lowest possible statistical uncertainty of the temperature measurements depending on the background are presented. While the passband of the second rotational Raman channel is changed, the passband of the first rotational Raman channel (low J) stays constant. ~~This first~~ The RR1 channel is already so close to the laser wavelength that further change to weaker signals would decrease the blocking of the elastically backscattered light in the signal to critical values.

Refined simulations to what ~~has~~ had already been described ~~in (~~by Radlach et al.~~,~~ (2008) were performed for the present laser wavelength and with the goal to find an optimum setting for the central wavelength of the second rotational Raman channel for high and

low background, respectively. In the following the central wavelength of the first rotational Raman signal detection channel is called CWL1 and the second CWL2 respectively. From Eq. (4), the 1-σ-statistical uncertainty of temperature measurements can be calculated for two close temperatures T_1 and T_2 with

$$\Delta T = \frac{\partial T}{\partial Q}\Delta Q \approx \frac{(T_1 - T_2)}{(Q_1 - Q_2)} Q \sqrt{\frac{P_{\mathrm{RR1}} + P_{\mathrm{B1}}}{P_{\mathrm{RR1}}^2} + \frac{P_{\mathrm{RR2}} + P_{\mathrm{B2}}}{P_{\mathrm{RR2}}^2}}. \tag{10}$$

A simulation of the spectrum at two temperatures T_1 and T_2 five kelvin apart combined with the filter transmission curves gives the ratio Q of the two channels. Scaling parameters of the background are the ratio of the background per 0.1 nm filter bandwidth and the intensity $P_{\mathrm{J}}^{\mathrm{max}}$ of the strongest line of the rotational Raman spectrum (Radlach, 2009). This gives as background

$$P_{\mathrm{B}} = S \frac{\Delta\lambda_{\mathrm{FWHM}}}{0.1\mathrm{nm}} P_{\mathrm{J}}^{\mathrm{max}}. \tag{11}$$

For the scaling factor S we chose 1 in the high-background case and 0 in the low-background case. As the intensity of the Raman signal depends on height but the background is constant for all height bins of a profile, the scaling factor S changes for the different heights of a measured profile and, of course, with the solar background and thus latitude, time of the day, and season as well as the laser power and receiver efficiency of the lidar system. ~~At~~ During daytime, S will be nearly 0 at low altitudes for a well-designed high-power lidar with high signal to background ratio, but S will increase quickly with altitude as the signal intensity decreases. With optimizations to $S = 0$ and $S = 1$, one is even prepared for high background conditions e.g. near cumulus clouds at noon. ~~We~~ It was found that larger values for S do not change the optimum central wavelengths significantly compared to $S = 1$. But as detailed in the following, the differences between $S = 0$ and $S = 1$ are significant which is the motivation for the new switch.

In Fig. 5 the results of the simulations are presented for both high and low background for temperature regimes of 180, 240, 270, and 300 K. The simulation was performed assuming

a beam divergence of 0.45° on the interference filters in the receiver which modifies the filter transmission curves accordingly. The beam divergence was chosen in agreement with the divergence in the polychromator in the current setup. For divergence values between 0.1° and 1.0°, the optimum wavelengths and iso-lines shift by 0.01 nm and 0.02 nm, respectively. The relative uncertainty ΔT is normalized to the smallest value in each case. The values of ΔT are of course lower at night than at day but this simulation is made to find an optimum setting within each regime and comparing than the optimum settings. The central wavelengths of the first filter are limited to 354.2 nm and smaller ~~values due to otherwise too low blocking of~~ to ensure that the elastic signal is blocked sufficiently for this channel.

~~We decided to select the pair of central wavelengths of~~ The central wavelengths were 354.15 nm for CWL1 and ~~353.35~~353.30 nm for CWL2 for high background conditions (H) for the measurements discussed here. With low background during night this setting is not ~~preferable~~ optimum, and therefore the pair of central wavelengths of 354.15 nm and 353.05 nm respectively was ~~selected~~ used for low background condition (L). We use correspondingly the angles of incidence already mentioned in Table 1. In Fig. 6, an overview of all these temperature regimes is given. One can see that the measurements with our settings are not more than 20 % higher than the minimum uncertainty for all temperatures between 240 and 300 K. But this is only achieved by the two settings for CWL2.

To be able to use the advantages of both wavelengths, it is crucial to be able to toggle between the two settings in a short time in order to avoid measurement gaps. Furthermore, the setting should be reproducible to avoid changes in calibration or overlap. This is realized by a filter holder which can be fixed by a pivot tooth at two positions. It was built by our workshop and tested on the campaign. Results are shown in Sect. 3.1.

3 Measurement examples

3.1 RR2 switch

To test the performance of the switch, ~~we made~~ a 24 h measurement ~~and changed~~ was made including changes between the high- and low-background setting (referred to hereafter as H and L). The switching time coincided with a radiosonde launch during nighttime. In general, ~~we define nighttime here~~ 'low background' conditions are here defined as the time where the background is small compared to the rotational Raman signals in ~~our~~ the altitude range of interest, i.e., between about half an hour after sunset and half an hour before sunrise. This was the case during the consecutive observation periods ~~where we had~~ with a radiosonde launch at 20:00 UTC and early in the morning. All in all, ~~we had therefore~~ there were three cases for the evaluation of the performance of the switch.

On average it took about 5 min to interrupt the data acquisition in a controlled way, change filter position, readjust the stray-light cover and restart the data acquisition. When changing from high- to low-background setting, the signal intensity in the second Raman channel decreases which results in a lower ratio Q (Fig. 7). But, as already discussed above, the relative sensitivity to temperature increases. The enhanced sensitivity is seen in Fig. 8, where the ratio between the two channels is normalized to the value at an arbitrary altitude (here ~~we chose that altitude~~ the altitude was chosen in which the temperature profile of the radiosonde was 273 K, which was 2.6 km). In this visualization the different slope can be seen, which is larger for L than for H.

Finally, ~~we compare~~ the Q vs. T curves from simulation and experiment (Fig. 9) are compared. For the experimental data, ~~we attributed~~ Q values were assigned to T values of the radiosonde ~~in~~ at the same height. The simulation calculates the resulting Q for temperatures from 240 to 300 K in 1 K steps ~~and includes~~ for the actual filter curves including the central wavelengths. For the low-background setting, simulation and experiment agree very closely ~~to~~ within the statistical error bars; for the high-background, ~~small deviations up to 3are found. But this deviation is only present in higher altitudes where the performance of the setting is not optimized ($T \approx 250$~~a deviation of <1.5 K ~~) and also the radiosonde~~

~~used to relate the altitude to a temperature can show deviations (sampling of~~ is found for Q values between 1.0 and 1.05. A comparison with Fig. 8 shows that this the altitude region where an inversion layer was found. An inversion layer can lead to differences between radiosonde and lidar measurement due to averaging of the lidar data and sampling of a different air mass~~). Therefore we can state a good~~ . The experimental determined Q is linked to the temperature values of the radiosounding, a deviation of 1 to 2 K therefore can be attributed to the inversion. As there are for all other temperatures only deviations within the 1-σ statistical uncertainties, we conclude that the agreement between experiment and simulation is good.

The statistical errors for different background values with ~~both~~ the two settings were calculated. ~~We used nighttime measurements and added~~ Night-time measurements were used and for the high background case background added according to a scaling factor of ~~exactly~~ $S = 1$ at 1 km. In comparison with actually measured background values at noon with or without cloud coverage the used background values are higher because ~~our rotational Raman signals~~ the Raman signals of the UHOH RRL are quite strong. Thus, the comparison shows the performance in circumstances which can be considered a worst case scenario.

Figure 10 shows the statistical errors with low background (measurement from 20:00 UTC, 20 min average) and both settings. ~~Like~~ Even at night-time, there is a background of around 1 photon per bin for the integrated average over 500 laser pulses. Therefore S is not strictly equal to zero, but, in this case, S was less than 0.1 up to 2.1 km for the L setting and up to 3.2 km for the H setting. S equal 1 was reached at 4.3 km and 6.6 km respectively. As expected, the setting L shows smaller errors for low altitudes and is favorable up to 7 km. The simulated error for high background is shown in Fig. 11. ~~Absolute values are higher than with~~ The absolute error values are in this case higher than in case of low background. Below 1 km, S is ~~smaller~~ less than 1 which results in a better performance of the low background setting than the high background setting. Above 1 km, S is larger than 1 and the statistical errors are smaller with the high-background configuration.

To show the advantage of the new setting the ratio between the error with high background setting ΔT_{HBS} and the error with low background setting ΔT_{LBS} was calculated for the different background conditions respectively. The result is shown in Fig. 12. Using setting L is favorable during ~~night~~ night-time up to a height of 7 km ~~. This change in advantage from L to H with low background was expected from the simulation. There the H setting shows less uncertainty at low temperatures than the L setting.In low altitudes,~~ like already seen in Fig. 10. ΔT is reduced by 70% for altitudes between 1 and 2 km. Above this altitude the advantage of L over H decreases. For high altitudes, H is still better than L even at night (see Fig. 6 for low temperatures <240 K) This behavior is explained by the fact that the background factor S will be ≥ 1 in such altitudes. During daytime the signal intensity is high ~~enough so that $S < 1$~~so that $S < 1$ in low altitudes. Here both settings show similar statistical errors with ~~small advantages of~~ advantages of up to 20% (at 0.5 km) of the low background configuration. With $S = 1$ at 1 km, setting H is ~~in advantage~~ advantageous above this altitude.

Because the background factor S assumed in the simulations is higher than in reality for the strong signals ~~we obtain with our system~~ which are obtained with the UHOH RRL during cloud-free conditions, the altitude where the high background setting shows ~~advantages is found for us even at higher altitudes than~~ an advantage lies above 1 km unless clouds cause higher background by scattering sunlight. By applying the setting H in daytime, ~~we can guarantee~~ it can be guaranteed even under these very high background conditions a good to optimum measurement performance. It is interesting to note that also smaller laser power would result in higher values of S ~~. Thus our~~ for all background levels. Thus this optimization approach can be used to adapt the optimum receiver passbands to the system parameters of other lidars.

3.2 Temperature gradient and humidity

Figure 13 shows the water vapor mixing ratio ~~MR~~ (MR) and the temperature gradient during a 25 h measurement period between 18 May 2013 15:00 UTC and 19 May 2013 16:00 UTC. The lidar was pointing vertically during this time period. The setting of IF3 was changed at

20:00 UTC and at 5:00 UTC the next morning. MR data are shown with one-minute averaging. A 78 m gliding height average was applied to the data. The boundary layer top can be seen due to the gradient between the moist boundary layer and the lower values of MR in the free troposphere. The time series starts at 15:00 UTC and the boundary layer is still convective at this time. The top of the boundary layer can be found around at 1.6 km. With sunset at 19:22 UTC there is a transition to a stable nocturnal boundary layer. Also a residual layer with a mixing ratio of 3 g kg^{-1} can be observed above the boundary layer with around 6 g kg^{-1} up to 1 km. Due to the lower solar background a moist layer between 2 and 3 km can be observed during night. Sunrise is at 03:39 UTC, ~~what~~ which can be seen by the increase of noise around this time. From 10:00 UTC on the convective boundary layer starts to increase in altitude and shows higher values of mixing ratio (around 8 g kg^{-1}) than the day before. The height of the boundary layer top does not change significantly from 1.5 km after 14:00 UTC.

For the altitude region marked with the white box the temperature gradient is shown in the lower panel. The resolution of temperature gradient data is 30 min and 105 m. These values have been chosen to monitor the mean boundary layer height continuously. A high positive gradient ~~is result of an inversion on top of a layer. Here we~~ indicates a temperature inversion. Here one can see a positive gradient at 1.5 km with a value around 1.2 K/100 m between 17:30 and 19:00 UTC which is ~~surprising~~ remarkable to see in the late afternoon just before sunset. We would have not expected to find such high values in this altitude so late in the day. After sunset the gradient ~~gets weaker and splits~~ became weaker and split to the top of the nocturnal boundary layer and a residual layer at 1.7 km which already was observed with the water vapor mixing ratio time series. The residual layer ~~stays~~ stayed at this altitude during the whole measurement period. From 03:00 till 07:00 UTC another inversion can be seen between 1 km and 1.3 km. A strong inversion ~~is~~ was present on top of the growing convective boundary layer 10:00 till 15:00 UTC. This demonstrates that with temperature gradient layers can be identified and observed during longer time periods.

Figure 14 shows the time period from 17:30 to 18:30 UTC in more detail. The water vapor mixing ratio in the upper left panel has the same resolution as in Fig. 13.The temperature

gradient is shown with two different temporal resolutions, 50 s gliding average over 10 s profiles on the right upper panel, 5 min on the left lower panel. The statistical uncertainty of the temperature gradient can be seen in the right lower panel. While the statistical error of the 5 minute average is 1.1 K/100m in 1.5,~~the water vapor mixing ratio has the same resolution as in Fig. 13.~~ km altitude, the 50 s average shows an error of 4 K/100m. Therefore it can be used to determine qualitatively the altitude of the highest gradient, but not to identify absolute values. The altitude of the positive gradient and the top of the moist layer agree well for the shown time period even in this high temporal resolution.

The profiles of temperature, potential temperature, temperature gradient and water vapor mixing ratio and their corresponding statistical uncertainties measured on 19 May 2013 between 13:00 and 13:30 UTC are shown in Fig. ~~15 with their corresponding statistical uncertainties.~~ 15. This time period near local noon was chosen because the highest background values during ~~this~~ the 25 h measurement period were found here; these examples thus illustrate the lower limit of the measurement performance with all other periods having smaller statistical uncertainties. For the temperature profiles an average of 167 raw data profiles was used and a gliding height average of 105 m was applied. A pressure profile measured by the radiosonde started at 13:00 UTC was used to calculate potential temperature. In the profiles of temperature, potential temperature and temperature gradient one can see the characteristics of a well-mixed boundary layer up to about 1100 m. In the interfacial layer above, differences between the measurements of both instruments can be identified. As the lidar measurement is an average over half an hour and the radiosonde profile is just a snapshot, this is reasonable. For the water vapor profile measured with the lidar (Fig. ~~15d~~15e) a 154 m gliding average was applied. The moist boundary layer, a very dry layer just above, and a second moist layer above 2 km were found. In the dry layer, the uncertainty of the water vapor Raman lidar measurement gets larger in absence of moisture due to the small water vapor Raman backscatter signal. In Fig. 15f the absolute and relative errors of the water vapor mixing ratio are shown. Of course, negative values of the water vapor mixing ratio are physically not possible. But in this case, they appear as measured values as a consequence of the small signal to noise ratio due to the small amount of water

vapor at this height resulting in a signal which was hardly statistically distinguishable from the daylight background. Note that the 1-σ statistical range indicates a probability of 68% that the real value in found within. We do not want to shift these values to 0 because if doing so, the mean of the data would be biased.

The profiles are shown with noise error bars derived by ~~Poisson statistics.~~Eq. 4. A detailed error analysis including errors derived by turbulence analysis is discussed by (Behrendt, et al., 2014).

3.3 Low-elevation pointing

In vertical pointing mode low heights cannot be observed due to overlap effects. These effects can be corrected down to a certain altitude, but in most cases a minimum altitude of 300 m in the case of water vapor mixing ratio or temperature can unfortunately not be overcome with ~~our~~ a single-telescope design. One solution for this problem is to perform measurements with small elevation angles. During the measurement shown in Fig. 16, the elevation angle was set to 10°. During HOPE, the measurement site was elevated ~~in respect of the surrounding~~ above its surroundings by 10 to 15 m. This has been taken into account when transferring range ~~in~~ to height above ground. The measurement geometry is illustrated in Fig. 17.

In Fig. ~~16a~~ 16 a comparison between the acquired lidar profile from 02:40 to 02:58 UTC and the radiosonde started at 03:00 UTC is shown. Raw data were treated like vertical acquired profiles and projected to the vertical for the comparison. A positive gradient is present below 100 m in the lidar profile, whereas in the radiosonde profile it is shifted by 50 m to higher altitudes. The lidar profile is corrected for the altitude of the surrounding terrain. Whereas the altitudes of the inversion differ, the slope of the temperature profiles is identical. So we conclude that the observations reveal indeed differences of the temperature inversion profile of the nocturnal boundary layer.

4 Summary and outlook

In this paper the performance of the Rotational Raman Lidar of University of Hohenheim during the HOPE campaign in April to May 2013 is presented.

To optimize the temperature measurements for both low and high background, a switch for the alignment of the interference filter for the second rotational Raman was implemented. It is possible to switch between the configurations in short time. The experimental data confirm the optimization simulations. The measurements proved the advantages of the new low background configuration up to 7 km during night measurements~~.~~, especially in altitudes under 4 km. An improvement of the statistical error up to 70% can be found. Depending on the actual background level present during a measurement, the low-background configuration is also favorable in ~~low altitudes in daytime due~~ altitudes under 1 km in daytime. Due to the high signal intensities of the UHOH RRL ~~. The high background setting shows low statistical error up to the top of the boundary layer even under high background conditions.~~ values of S less than 1 can be found in this altitude range. For larger background levels the improvement of the statistical error for using the H setting is up to 20%. The advantage is not as large when changing from H to L, but one should keep in mind that a reduction of the statistical uncertainty by 20% is equivalent to, e.g., an increase on laser power of 44%.

The simulation was performed with the system parameters of the UHOH RRL. Therefore some points have to be taken into account when the results shown here are to be transferred to other systems. To get the exact values for another system, the simulation has to be repeated with the specific system parameters. However, the shifts from the excitation wavelength will be similar for other RRL systems operated in the UV. Additionally, the desired wavelength pairs depend on the temperature range to be measured with the highest precision including the background level in relation to the signal intensity. Having all these factors in mind, one can estimate suitable wavelength pairs from Fig. 6.

Furthermore, the UHOH RRL was equipped with an additional channel to detect the vibrational Raman lines of water vapor and delivers now as a product the atmospheric water vapor mixing ratio of the atmospheric boundary layer and lower free troposphere in day and

night. As molecular reference signal a temperature independent combination of the two rotational Raman signals is used; not a vibrational Raman signal of nitrogen as commonly used. The statistical error depends on humidity. During daytime the lower two kilometers of the atmosphere can be observed with a ~~convenient~~ time and height averaging ~~e.g. of~~ 20 min and 154 m gliding average to achieve an absolute noise error less than 0.5 g kg^{-1}~~.~~ , which fulfills the requirements for boundary layer studies (Stull 1988). Time series of water vapor mixing ratio and temperature gradient over a 25 h period were shown and the diurnal changes in the boundary layer can be observed. Results from a low level measurement with capture of a strong inversion at 100 m show the capability to measure in a low altitude range above ground with the beam steering unit.

Acknowledgements. The HOPE campaign was funded by the German Research Ministry under the project number 01LK1212 A. We thank KIT and University of Cologne for performing the radiosonde launches.

References

Achtert, P., Khaplanov, M., Khosrawi, F., and Gumbel, J.: Pure rotational-Raman channels of the Esrange lidar for temperature and particle extinction measurements in the troposphere and lower stratosphere, Atmos. Meas. Tech., 6, 91–98, doi:10.5194/amt-6-91-2013, 2013.

Arshinov, J., Bobrovnikov, S., Serikov, I., Ansmann, A., Wandinger, U., Althausen, D., Mattis, I., and Müller, D.: Daytime operation of a pure rotational Raman lidar by use of a Fabry-Perot interferometer, Appl. Optics, 44, 17, 3593–3603, 2005.

Avila, G., Fernandez, J. M., Tejeda, G., and Montero, S.: The Raman Spectra and cross-sections of H_2O, D_2O, and HDO in the OH/OD-stretching regions, J. Mol. Spectrosc., 228, 38–65, 2004.

Balin, I., Serikov, I., Bobrovnikov, S., Simeonov, V., Calpini, B., Arshinov, Y., and van der Bergh, H.: Simultaneous measurement of atmospheric temperature, humidity, and aerosol extinction and backscatter coefficients by a combined vibrational-pure-rotational Raman lidar, Appl. Phys. B, 79, 775–782, 2004.

Behrendt, A.: Temperature Measurements with Lidar, Lidar: Range-Resolved Optical Remote Sensing of the Atmosphere, Springer, New York, 2005.

Behrendt, A. and Reichardt, J.: Atmospheric temperature profiling in the presence of clouds with a pure rotational Raman lidar by use of an interference-filter-based polychromator, Appl. Optics, 39, 1372–1378, 2000.

Behrendt, A., Nakamura, T., Onishi, M., Baumgart, R., and Tsuda, T.: Combined Raman lidar for the measurement of atmospheric temperature, water vapor, particle extinction coefficient, and backscatter coefficient, Appl. Optics, 36, 7657–7666, 2002.

Behrendt, A., Nakamura, T., and Tsuda, T.: Combined temperature lidar for measurements in troposphere, stratosphere and mesosphere, Appl. Optics, 14, 2930–2939, 2004.

Behrendt, A., Wulfmeyer, V., Riede, A., Wagner, G., Pal, S., Bauer, H., Radlach, M., Späth, F.: Three-dimensional observations of atmospheric humidity with a scanning differential absorption lidar, Proc. SPIE, 7475, 2009.

Behrendt, A., Pal, S., Aoshima, F., Bender, M., Blyth, A., Corsmeier, U., Cuesta, J., Dick, G., Dorninger, M., Flamant, C., Di Girolamo, P., Gorgas, T., Huang, Y., Kalthoff, N., Khodayar, S., Mannstein, H., Träumner, K., Wieser, A., and Wulfmeyer, V.: Observation of convection initiation processes with a suite of state-of-the-art research instruments during COPS IOP 8b, Q. J. Roy. Meteor. Soc., 137, 81–100, 2011.

Behrendt, A., Wulfmeyer, V., Hammann, E., Muppa, S. K., and Pal, S.: Profiles of second- to third-order moments of turbulent temperature fluctuations in the convective boundary layer: first measurements with rotational Raman lidar, Atmos. Chem. Phys. Discuss., 14,29019–29055, ~~submitted,~~doi::10.5194/acpd-14-29019-2014, 2014.

Bhawar, R., Di Girolamo, P., Summa, D., Flamant, C., Althausen, D., Behrendt, A., Kiemle, C., Bosser, P., Cacciani, M., Champollion, C., Di Iorio, T., Engelmann, R., Herold, C., Pal, S., Riede, A., Wirth, M., and Wulfmeyer, V.: The water vapour intercomparison effort in the framework of the convective and orographically-induced precipitation study: airborne-to-ground-based and airborne-to-airborne lidar systems, Q. J. Roy. Meteor. Soc., 137, 325–348, 2011.

Cooney, J.: Measurement of atmospheric temperature profiles by Raman Backscatter, J. Appl. Meteorol., 11, 108–112, 1972.

Corsmeier, U., Kalthoff, N., Barthlott, C., Aoshima, F., Behrendt, A., Di Girolamo, P., Dorninger, M., Handwerker, J., Kottmeier, C., Mahlke, H., Mobbs, S., Norton, E. G., Wickert, J., and Wulfmeyer, V.: Processes driving deep convection over complex terrain: a multi-scale analysis of observations from COPS IOP 9c, Q. J. Roy. Meteor. Soc., 137, 137–155, 2011.

Di Girolamo, P., Marchese, R., Whiteman, D. N., and Demoz, B. B.: Rotational Raman lidar measurements of athmospheric temperature in the UV, Geophys. Res. Lett., 31, L01106, doi:10.1029/2003GL018342, 2004.

Di Girolamo, P., Summa, D., and Ferretti, R.: Multiparameter Raman lidar measurements for the characterization of a dry stratospheric intrusion event, J. Atmos. Ocean. Tech., 26, 1742–1762, 2009.

Immler, F., Engelbart, D. and Schrems, O.: Fluorescence from atmospheric aerosol detected by a lidar indicates biogenic particles in the lowermost stratosphere, Atmos. Chem. Phys., 5, 345-355, 2005.

Kalthoff, N., Adler, B., Wieser, A., Kohler, M., Träumner, K., Handwerker, J., Corsmeier, U., Khodayar, S., Lambert, D., Kopmann, A., Kunka, N., Dick, G., Ramatschi, M., Wickert, J., and Kottmeier, C.: KITcube – a mobile observation platform for convection studies deployed during HyMeX, Meteorol. Z., 22, 6, 633–647, 2013.

Leblanc, T. and McDermid, I. S.: Accuracy of Raman lidar water vapor calibration and its applicability to longterm measurements, Appl. Optics, 30, 5592–5603, 2008.

Lenschow, D. H., Wulfmeyer, V., and Senff, C.: Measuring second-though fourth-order moments in noisy data, J. Atmos. Ocean. Tech., 17, 1330–1346, 2000.

Lenschow, D. H., Lothon, M., Mayor, S. D., and Sullivan, P. P.: A comparison of higher-order vertical velocity moments in the convective boundary layer from lidar with in situ measurements and LES, Bound.-Lay. Meteorol., 143, 107–123, 2012.

Mao, J., Hua, D., Wang, Y., Gao, F., and Wang, L.: Accurate temperature profiling of the atmospheric boundary layer using an ultraviolet rotational Raman lidar, Opt. Commun., 282, 3113–3118, 2009.

Melfi, S. H., Lawrence, J. D., McCormick, M. P.: Observation of Raman scattering by water vapor in the atmosphere, Appl. Phys. Lett., 15, 9, 295–297, 1969.

Muppa, S. K., Behrendt, A., Späth, F., Wulfmeyer, V., Metzendorf, S., and Riede, A.: Turbulent humidity fluctuations in the convective boundary layer: case studies using DIAL measurements, ~~Atmos. Chem. Phys., in preparation~~Bound. Lay. Meteorol., submitted, 2014.

Newsom, R. K., Turner, D. D., Mielke, B., Clayton, M., Ferrare, R., and Sivaraman, C.: Simultaneous analog and photon counting detection for Raman lidar, Appl. Optics, 20, 3903–3914, 2009.

Pal, S., Behrendt, A., and Wulfmeyer, V.: Elastic-backscatter-lidar-based characterization of the convective boundary layer and investigation of related statistics, Ann. Geophys., 28, 825–847, doi:10.5194/angeo-28-825-2010, 2010.

Radlach, M.: A scanning eye-safe rotational Raman lidar in the ultraviolet for measurements of tropospheric temperature fields, doctoral thesis, Stuttgart, 2009.

Radlach, M., Behrendt, A., and Wulfmeyer, V.: Scanning rotational Raman lidar at 355 nm for the measurement of tropospheric temperature fields, Atmos. Chem. Phys., 8, 159–169, doi:10.5194/acp-8-159-2008, 2008.

Schwitalla, T. and Wulfmeyer, V.: Radar data assimilation experiments using the IPM WRF Rapid Update Cycle, Meteorol. Z. 1, 79–102, 2014.

Schotland, R. M.: Errors in the lidar measurement of atmospheric gases by differential absorption, J. Appl. Meteorol., 13, 71–77, 1974.

Senff, C., Bösenberg, J., and Peters, G.: Measurements of water vapor flux profiles in the convective boundary layer with lidar and radar-RASS, J. Atmos. Ocean. Tech., 11, 85–93, 1994.

Sherlock, V., Garnier, A., Hauchecorne, A., and Keckhut, P.: Implementation and validation of a Raman lidar measurement of middle and upper tropospheric water vapor, Appl. Optics, 27, 5838–5850, 1999.

Späth, F., Behrendt, A., Muppa, S. K., Metzendorf, S., Riede, A., and Wulfmeyer, V.: High-resolution atmospheric water vapor measurements with a scanning differential absorption lidar, Atmos. Chem. Phys. ~~, in preparation.~~Discuss., 14, 29057-29099, 2014.

Stevens, B. and Bony, S.: What are climate models missing?, Science, 340, 1053–1054, 2013.

Stull, R. B.: An Introduction to Boundary Layer Meteorology, Springer, Heidelberg, New York, 1988.

Su, J., McCormick, M. P., Wu, Y., Lee III, R. B., Lei, L., Liu, Z., and Leavor, K. R.: Cloud temperature measurement using rotational Raman lidar, J. Quant. Spectrosc. Ra., 125, 45–50, 2013.

Turner, D. D. and Goldsmith, J. E. M.: Twenty-four-hour Raman lidar water vapor measurements during the atmospheric radiation measurement program's 1996 and 1997 water vapor intensive observation periods, J. Atmos. Ocean. Tech., 16, 1062–1076, 1999.

Turner, D. D., Ferrare, R. A., Wulfmeyer, V., and Scarino, A. J.: Aircraft evaluation of ground-based Raman lidar water vapor turbulence profiles in convective mixed layers, J. Atmos. Ocean. Tech., 31, 1078–1088, 2014a.

Turner, D. D., Wulfmeyer, V., Berg, L. K., and Schween, J. H.: Water vapor turbulence profiles in stationary continental convective mixed layers, J. Geophys. Res., accepted, 2014b.

Wagner, G., Behrendt, A., Wulfmeyer, V., Späth, F., and Schiller, M.: High-power Ti:sapphire laser at 820 nm for scanning ground-based water–vapor differential absorption lidar, Appl. Optics, 52, 11, 2454–2469, 2013.

Whiteman, D. N., Melfi, S. H., and Ferrare, R. A.: Raman lidar system for the measurement of water vapor and aersosols in the Earth's atmosphere, Appl. Optics, 31, 16, 3068–3082, 1992.

Whiteman, D. N., Demoz, B., di Girolamo, P., Comer, J., Veselovskii, I., Evans, K., Wang, Z., Sabatino, D., Schwemmer, G., Gentry, B., Lin, R-F., Behrendt, A., Wulfmeyer, V., Browell, E., Ferrare, R., Ismail, S. and Wang, J.:Raman Lidar Measurements during the International H2O Project. Part II: Case Studies, J. Atmos. Oceanic Technol., 23, 170-183, 2006.

Wulfmeyer, V.: Investigation of turbulent processes in the lower troposphere with water-vapor DIAL and Radar-RASS, J. Atmos. Sci., 56, 1055–1076, 1999a.

Wulfmeyer, V.: Investigations of humidity skewness and variance profiles in the convective boundary layer and comparison of the latter with large eddy simulation results, J. Atmos. Sci., 56, 1077–1087, 1999b.

Wulfmeyer, V. and Bösenberg, J.: Ground-based differential absorption lidar for water-vapor profiling: assessment of accuracy, resolution, and meteorological applications, Appl. Optics, 37, 18, 3825–3844, 1998.

Wulfmeyer, V. and Feingold, G.: On the relationship between relative humidity and particle backscattering coefficient in the marine boundary layer determined with differential absorption lidar, J. Geophys. Res., 105, 4729–4741, 2000.

Wulfmeyer, V., Pal, S., Turner, D. D., and Wagner, E.: Can water vapour Raman lidar resolve profiles of turbulent variables in the convective boundary layer?, Bound.-Lay. Meteorol., 136, 253–284, 2010.

Zeyn, J., Lahmann, W., and Weitkamp, C.: Remote daytime measurements of tropospheric temperature profiles with a rotational Raman lidar, Opt. Lett., 21, 16, 1301–1303, 1996.

Table 1. Parameter of interference filters. AOI: angle of incidence, CWL: central wavelength, FHWM: full width at half maximum.

	IF0	IF1	IF2a	IF2b	IF3	IF4
AOI, deg	0	4.8	6.0	6.0	~~4.5~~4.8/6.2	3.9
CWL, nm	355	354.8	354.15	354.15	~~353.35~~353.30/353.05	407.7
FWHM	8.5	0.3	0.3	0.3	0.5	0.3
Peak Transmission	0.56	0.62	0.53	0.65	0.52	0.75
Refl. at 354.8 nm		< 0.1				
Transm. at 354.8 nm	0.56	0.62	$<$ 1E-3	$<$ 1E-3	$<$ 1E-6	$<$ 1E-7

Table 2. Signal raw resolution.

Raw data	Temporal resolution	Spatial resolution	Recording Mode
Elastic signal	10 s	3.75 m	Analog + ~~photocounting~~ photon-cou
	10 s	37.5 m	photon-counting
	1 s	3 m	Analog
Rotational Raman 1	10 s	3.75 m	Analog + ~~photocounting~~ photon-cou
	10 s	37.5 m	photon-counting
Rotational Raman 2	10 s	3.75 m	Analog + ~~photocounting~~ photon-cou
	10 s	37.5 m	photon-counting
Vibrational Water Vapor	10 s	3.75 m	Analog + ~~photocounting~~ photon-cou

Table 3. Relative statistical temperature error for the high- and low-background setting of the center wavelength CWL2 of the interference filter of the second (high J) rotational Raman channel (H and L, respectively). S is the scaling factor for the background level (see text for details). While $S = 0$ stands for no background, $S = 1$ characterizes high background conditions. The resulting relative errors for the selected configurations are bold. With the optimized settings for CWL2 the statistical errors are not exceeding 20 % higher values than the absolute optimum for atmospheric temperatures between 240 and 300 K.

	$S = 0$				$S = 1$			
CWL2	180 K	240 K	270 K	300 K	180 K	240 K	270 K	300 K
~~353.35~~ 353.30 (H)	~~1.24~~1.25	~~1.29~~1.27	~~1.35~~1.31	~~1.54~~1.37	1.52	**1.17**	**1.13**	~~1.13~~**1.14**
~~352.95~~ 353.05 (L)	1.36	**1.13**	**1.10**	**1.10**	3.46	1.70	1.39	1.21

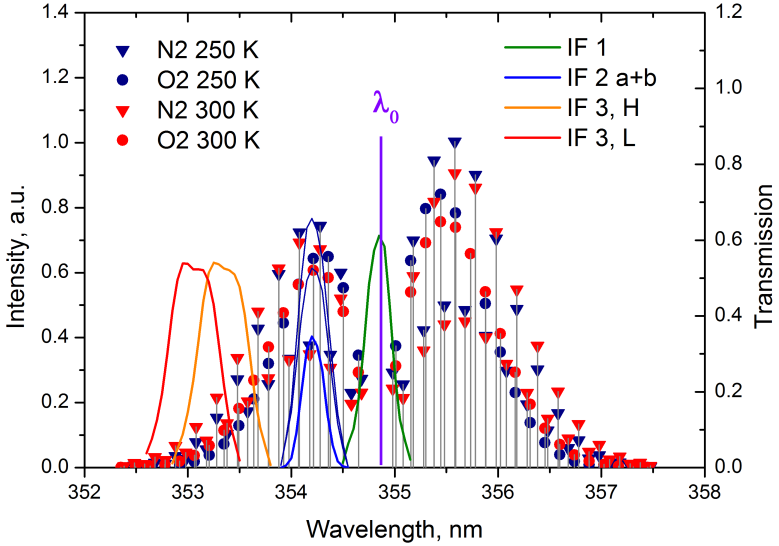

Figure 1. Rotational Raman spectrum of atmospheric nitrogen and oxygen for an excitation wavelength λ_0 of 354.83 nm and for two temperatures (250 and 300 K). Transmission curves of the interference filters are shown for comparison. Although the Stokes lines ($\lambda > \lambda_0$) are more intense, anti-Stokes lines ($\lambda < \lambda_0$) are used by us to avoid possible measurement errors due to fluorescence (Immler et al. 2005). For IF3, the filter positions for both the low- and high-background settings are shown (L and H, respectively).

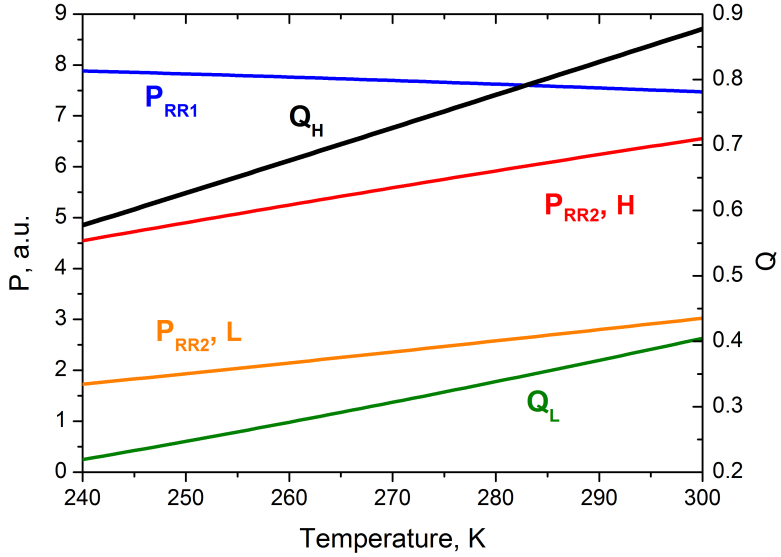

Figure 2. Simulated signal intensities for the filter configurations shown in Fig. 1: rotational Raman signal intensities for the H and L setting and corresponding ratios $Q = P_{\mathrm{RR2}}/P_{\mathrm{RR1}}$.

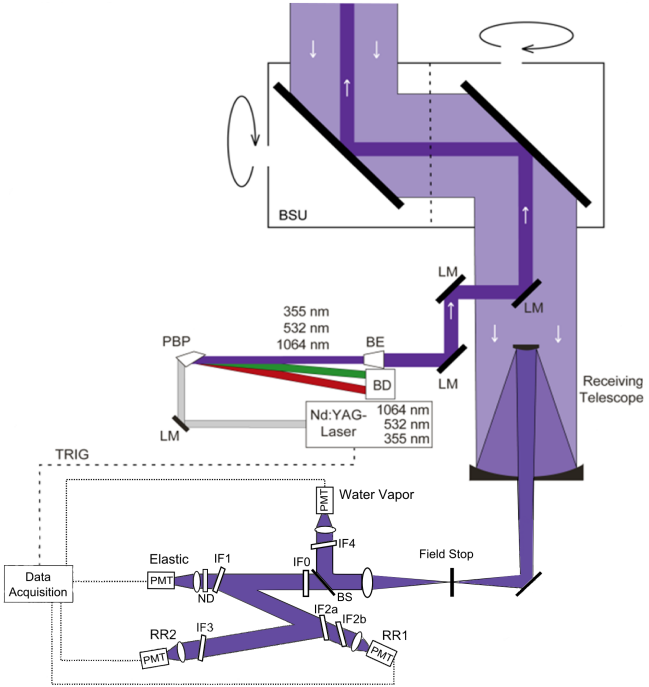

Figure 3. Setup of the rotational Raman lidar of University of Hohenheim. LM stands for laser mirror and the wavelengths are separated by a ~~Pellin-Broca-Prism~~Pellin-Broca-prism. Whereas 532 and 1064 nm are sent to a beam dump (BD), 355 nm is expanded by a beam expander (BE) and sent to the atmosphere through the beam steering unit (BSU). Angles in the polychromator are enlarged for clarity. IF0 is a daylight oppressing filter (see Table 1 for details). IF1 to IF4 are the interference filters, BS is a beam splitter to separate the vibrational Raman lines from the elastic backscattered and rotational Raman signal. In front of the elastic channel a neutral density filter (ND) is mounted. Photomultipliers are marked with PMT.

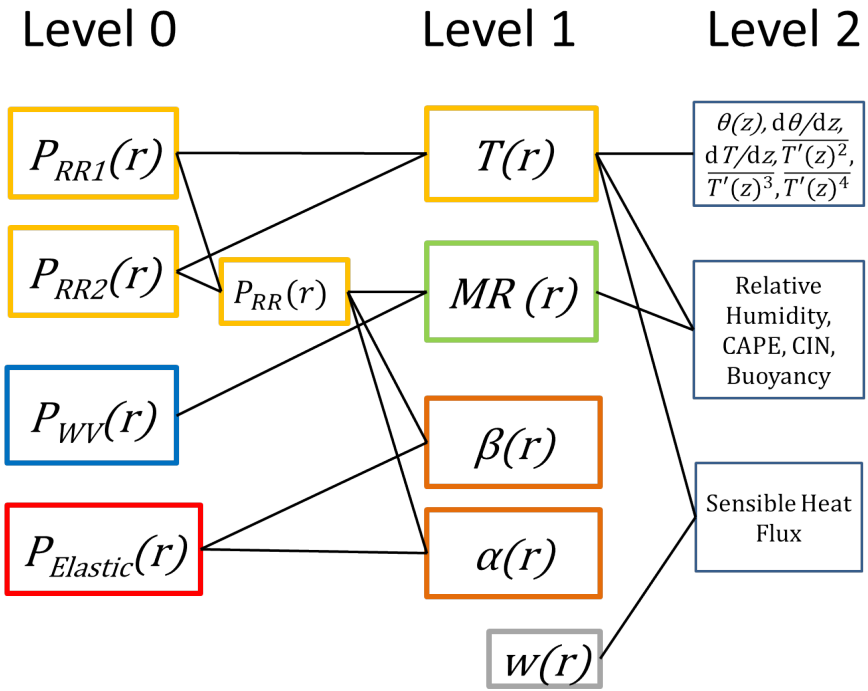

Figure 4. Diagram of the data products. Level 0 data are the background corrected rotational Raman signals (yellow), the vibrational Raman signal of water vapor (blue) and the elastic backscatter signal (red). A ~~temperature independent~~ temperature-independent reference signal P_{RR} is obtained from the temperature-dependent rotational Raman signals. Level 1 data products are temperature T, water vapor mixing ratio MR, particle backscatter coefficient β and particle extinction coefficient α. Higher-level products derived from level 1 data: potential temperature θ, gradient of temperature and potential temperature, higher moments of turbulent temperature fluctuations T', relative humidity, buoyancy, CAPE, and CIN. For deriving the sensible heat flux, profiles of the vertical wind w, e.g. from a Doppler lidar, are used.

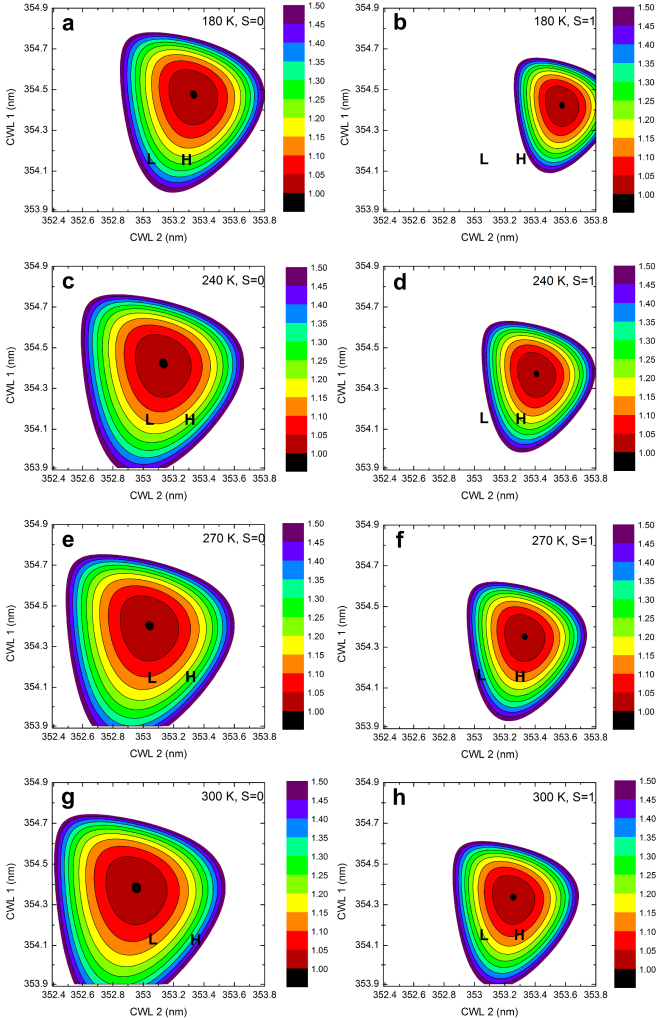
a
180 K, S=0
b
180 K, S=1
c
240 K, S=0
d
240 K, S=1
e
270 K, S=0
f
270 K, S=1
g
300 K, S=0
h
300 K, S=1
L
H
CWL 1 (nm)
CWL 2 (nm)
354.9
354.7
354.5
354.3
354.1
353.9
352.4 352.6 352.8 353 353.2 353.4 353.6 353.8
1.50
1.45
1.40
1.35
1.30
1.25
1.20
1.15
1.10
1.05
1.00

Figure 5. Statistical temperature uncertainty ΔT for different central wavelengths (CWL) of the RR filters. **(a)**, **(c)**, **(e)** and **(g)** without background ($S = 0$), **(b)**, **(d)**, **(f)** and **(h)** with background ($S = 1$). H denotes the configuration selected for high background measurements, L the configuration for low background measurements. The uncertainty values were normalized to the smallest value of each plot. The laser wavelength is 354.83 nm.

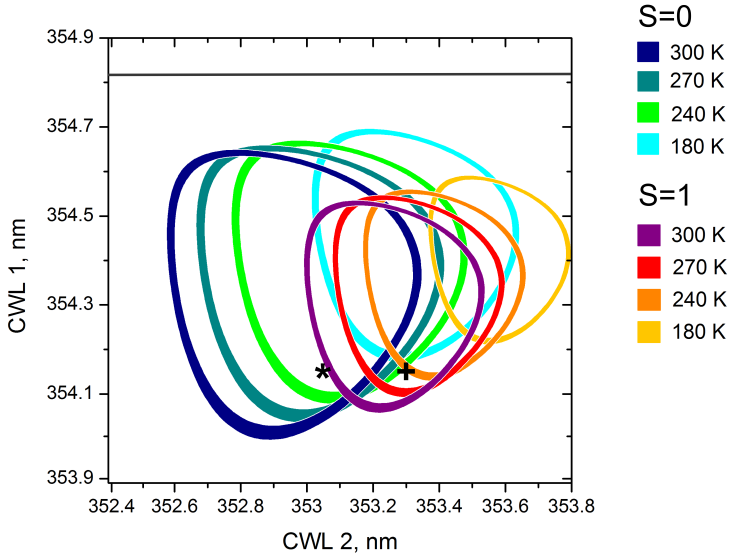

Figure 6. Overview of all cases shown in Fig. 5. The outer and inner borders of the rings mark 1.20 and 1.17 relative uncertainty, respectively. The selected configurations for high and low-background conditions (marked with + and *, respectively) show lower relative uncertainties than 1.2 for all temperatures between 240 and 300 K (see also Table 3). The gray line marks the laser wavelength.

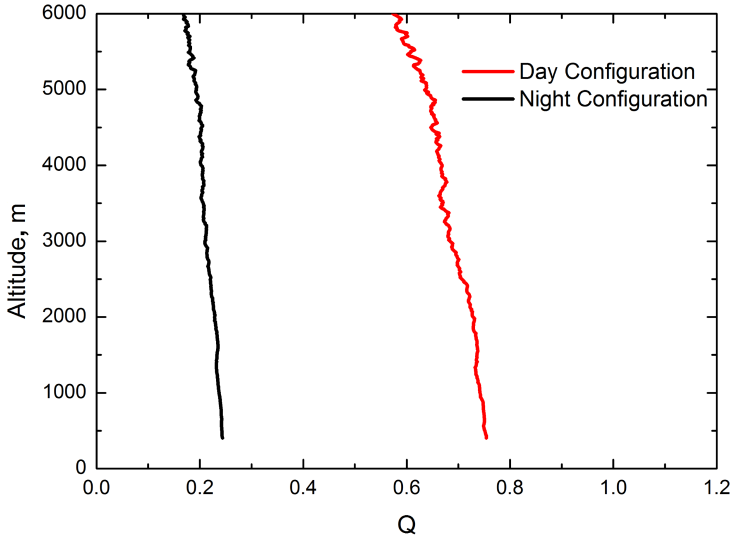

Figure 7. Measured ratio Q of the rotational Raman signals with the high- and low-background setting, H and L respectively, at night. The data for the setting H were collected between 19:38 and 19:58 UTC on 18 May 2013; data for the setting L just afterwards between 20:05 and 20:25 UTC. The intensity of the RR2 signal decreased by switching to L, hence the smaller ratio Q. The rotational signals were smoothed with a gliding average of 105 m height before the ratio was calculated.

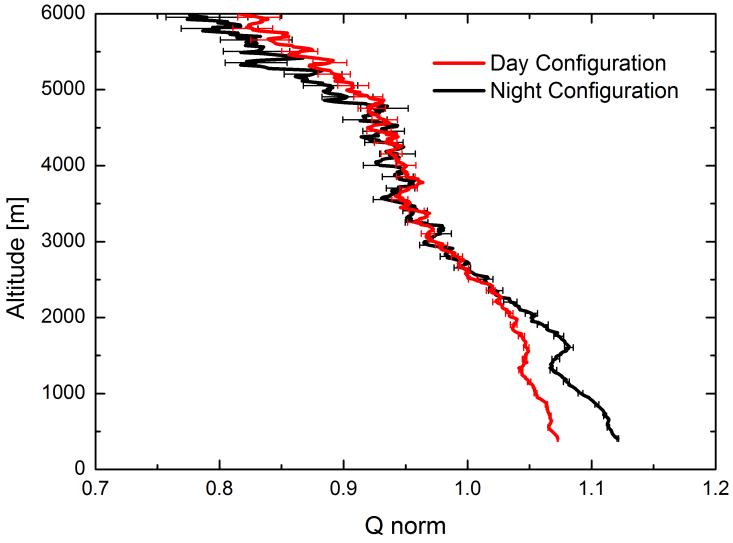

Figure 8. Same as Fig. 7 but normalized to 1 at a height of 2.6 km to illustrate the higher relative sensitivity of the low-background setting. Error bars show the statistical uncertainties.

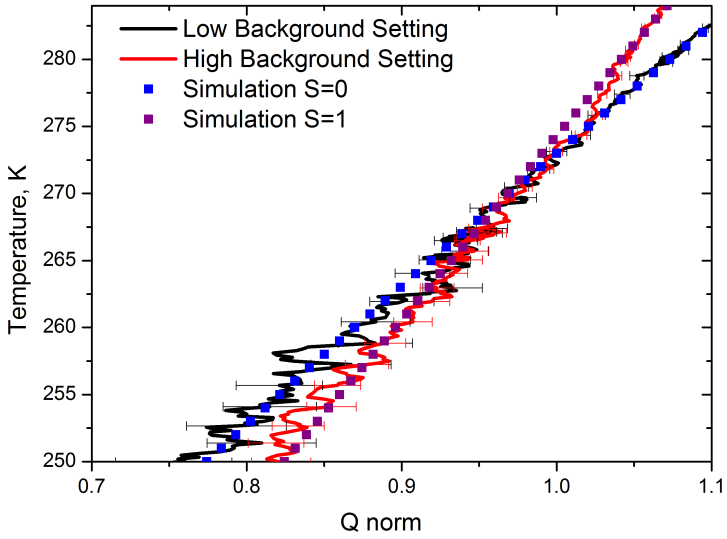

Figure 9. Same as Fig. 8 but against radiosonde temperature at the same height. In addition to the measurements, simulation data for the two settings are shown. In red and black are the measured values for Q with the statistical error, in blue and violet the corresponding simulation.

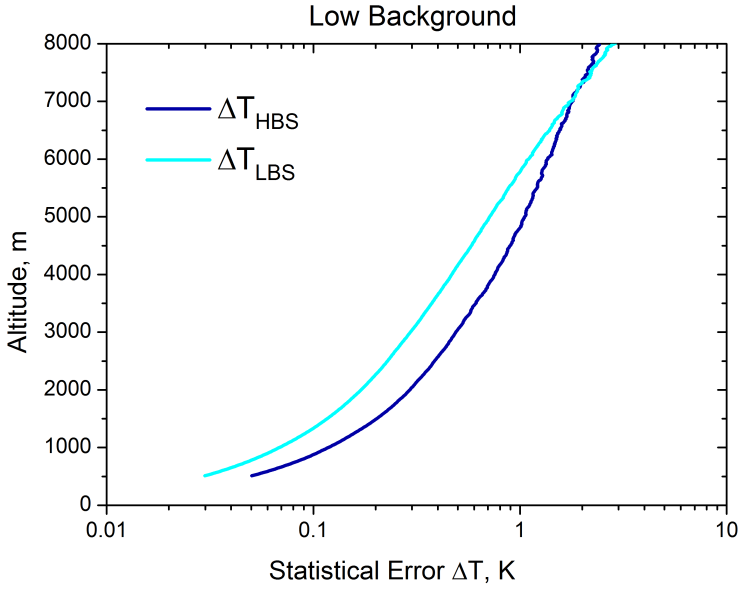

Figure 10. Comparison of the statistical error of the temperature measurements with both settings, ΔT_{HBS} and ΔT_{LBS} at low background conditions. The profiles were derived from data collected during about 20 min (55 000 laser shots) and with 105 m gliding average. Above 7 km altitude, the high background configuration shows smaller errors due to the lower atmospheric temperatures in these heights and also the decrease in signal-to-noise ratio.

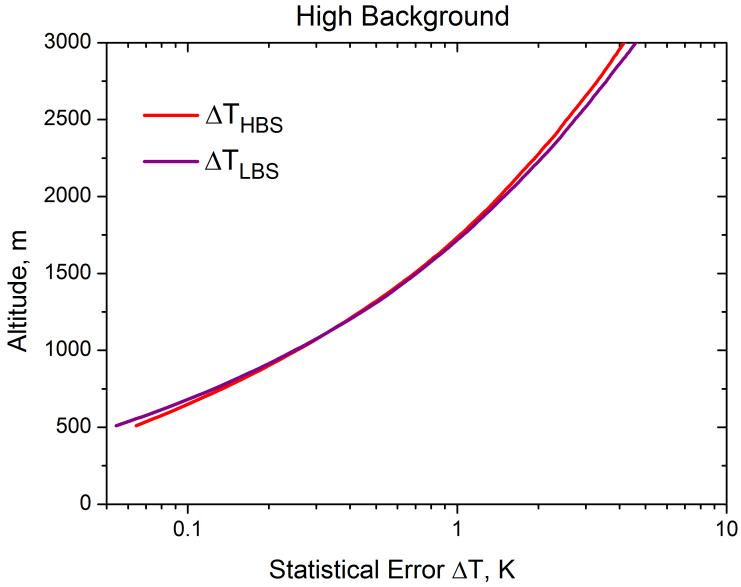

Figure 11. Same as Fig. 10 but for high background conditions (S = 1 in 1 km altitude). The high-background setting is superior for measurements above 1 km altitude.

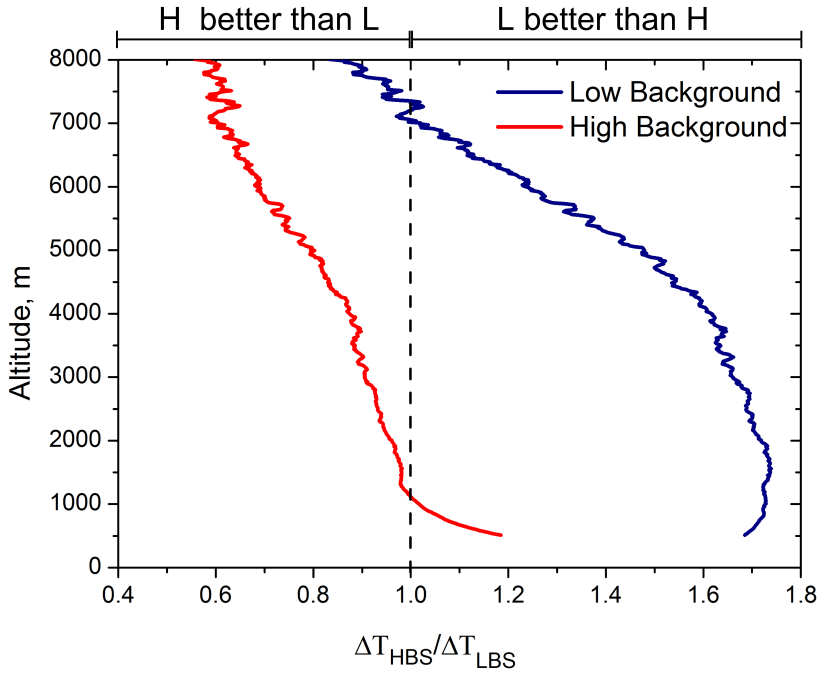

Figure 12. Ratio of high-background-setting uncertainties ΔT_{HBS} to low-background-setting uncertainties ΔT_{LBS}. A ratio above 1 shows better performance ~~of~~ for the low-background setting compared to the high-background setting. In cases with no background, this advantage is clearly significant ~~in~~ at lower altitudes but decreases with height. On the other hand, the high-background setting is superior already above 1 km in high background conditions. But it should be noted that the altitude where the high-background setting becomes preferable depends on the signal-to-background ratio.

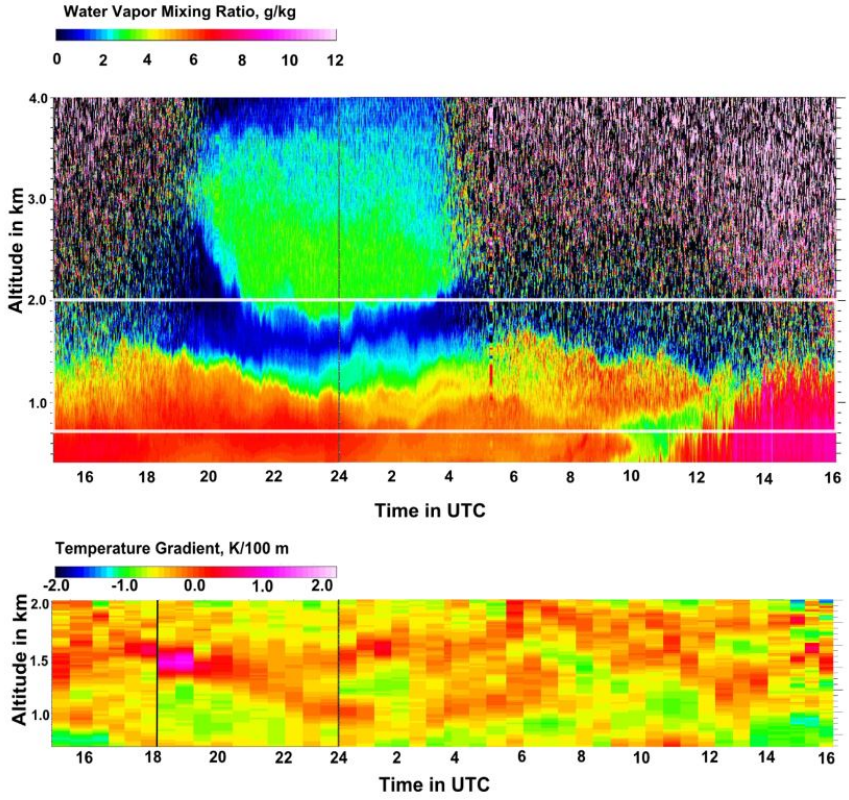

Figure 13. Time series of the water vapor mixing ratio (upper panel) and temperature gradient (lower panel) measured between 15:00 UTC on 18 May 2013 and 16:00 UTC on 19 May 2013. The white lines in the lower panel mark the height range of the data in the upper panel.

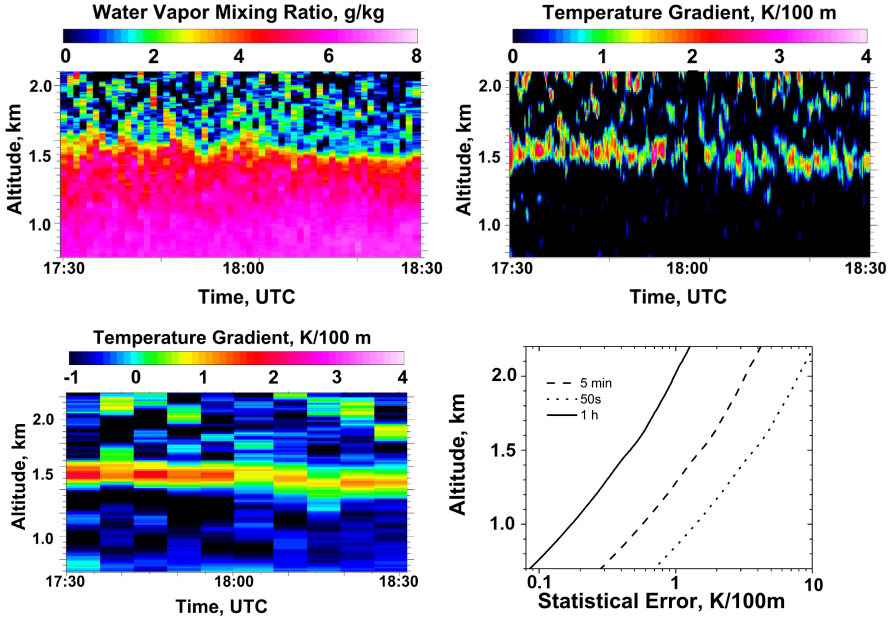

Figure 14. Detail from Fig. 13 of the time period from 17:30 to 18:30 UTC on 18 May. Left upper panel water vapor mixing ratio with 1 minute resolution, left lower panel temperature gradient with 5 minute and left upper panel with 10 s profiles and 50 s gliding time average, ~~right one minute water vapor profiles~~respectively. Right lower panel statistical error of temperature gradient measurements.

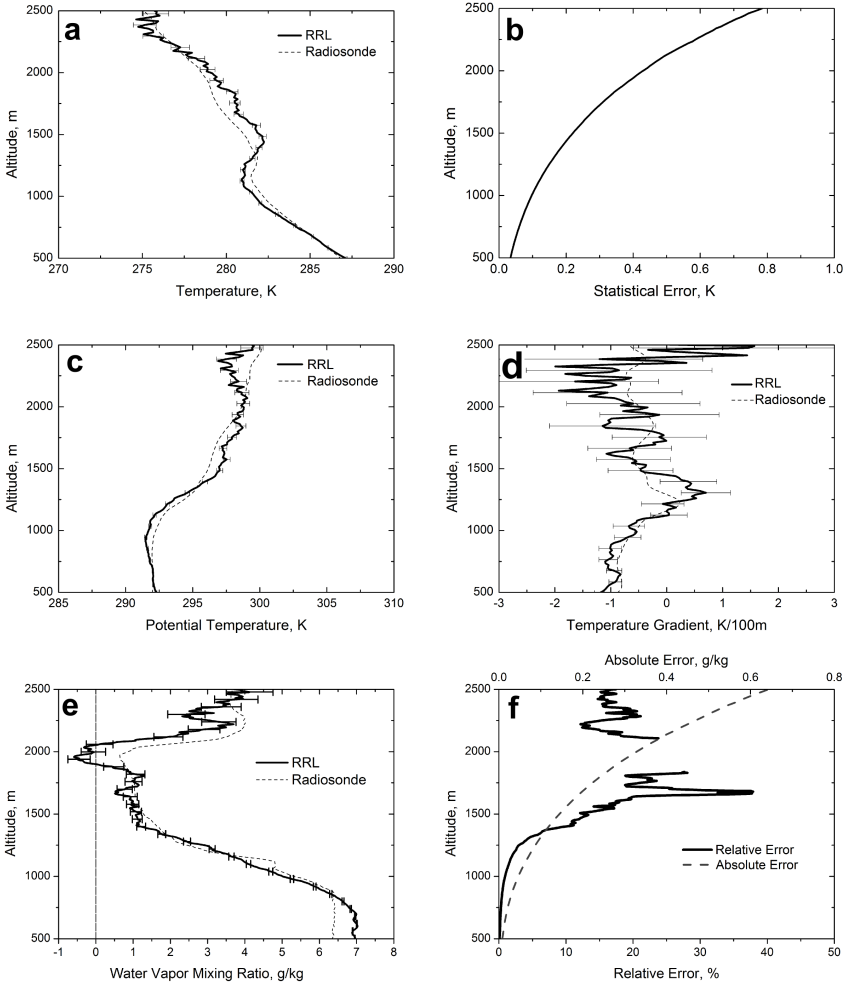
a
RRL
Radiosonde
Altitude, m
Temperature, K
b
Statistical Error, K
c
Potential Temperature, K
d
Temperature Gradient, K/100m
e
Water Vapor Mixing Ratio, g/kg
f
Absolute Error, g/kg
Relative Error
Absolute Error
Relative Error, %

Figure 15. Measurements of the UHOH RRL between 13:00 and 13:30 UTC on 19 May 2013 with data of a local radiosonde launched at 13:00 UTC (dashed) for comparison. **(a)** Temperature **(b)** ~~potential~~ statistical temperature error **(c)**potential temperature ~~gradient~~ **(d)** temperature gradient **(e)** water vapor mixing ratio **(f)** absolute and relative error of water vapor mixing ratio. Values of absolute error in the height range where the mixing ratio shows negative values are omitted. Error bars show the statistical errors of the lidar data. Altitudes below 500 m are affected by non-total overlap and are therefore not shown.

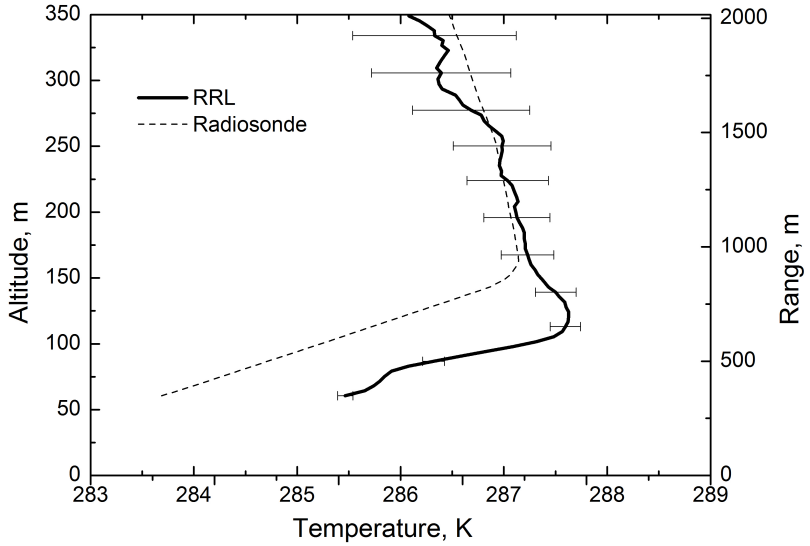

Figure 16. Results of low-elevation measurements: temperature measured with the UHOH RRL and a radiosonde (RS) against height a.g.l. The lidar data were collected from 02:40 to 02:57 UTC on 28 May 2013. The radiosonde measurement was started at 03:00 UTC. The altitude for the lidar profile is calculated from the range and corrected for topography. Lidar data at altitudes below 50 m are affected by overlap effects.

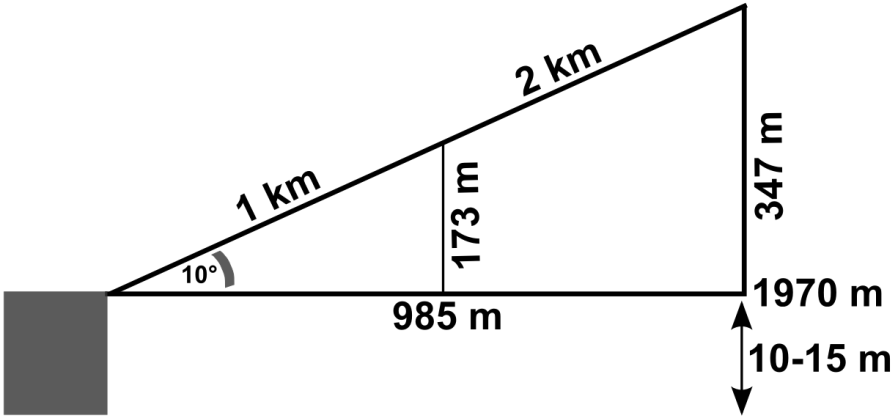

Figure 17. Illustration of the measurement geometry of Fig. 16.